The Astrophysical Journal, 630:596–614, 2005 September 1

OBSERVATIONS OF SEPARATOR RECONNECTION TO AN EMERGING ACTIVE REGION

D. W. Longcope, D. E. McKenzie, J. Cirtain, and J. Scott
Department of Physics, Montana State University, Bozeman, MT 59717-3840
Received 2004 October 6; accepted 2005 May 14

ABSTRACT

Extreme-ultraviolet (EUV) observations of an emerging active region are used to study separator reconnection in the corona. We identify each EUV loop connecting the emerging polarity to a nearby existing active region over the 41 hr period beginning at emergence onset. Their geometrical resemblance to post-reconnection field lines from a magnetic model of the active region pair implicates separator reconnection in their production. While some reconnection is evident within 7 hr of emergence onset, the most intense period occurs after a 1 day delay. The sum of cross sections of all observed loops accounts for only one-fifth of the transferred magnetic flux predicted by the model. We suggest that the remaining loops remain at temperatures too high, or at densities too low, to be detected in our EUV data. The most intense reconnection requires as much as 10^9 V along the coronal separator; however, the observed loops suggests that the flux is transferred as discrete bundles of $\sim 4 \times 10^{18}$ Mx each. The reconnection appears to directly dissipate only a small fraction of the energy released, while the rest is dissipated within the post-reconnection flux over the ensuing 6 or more hours the loops remain visible. The net energy released, and ultimately dissipated, is consistent with the amount that could be stored magnetically during the 24 hr delay between emergence and reconnection.

Subject headings: Sun: filaments — Sun: flares — Sun: magnetic fields — Sun: UV radiation

1. INTRODUCTION

Magnetic reconnection has been proposed to explain a wide variety of coronal activity including flares (Sweet 1958), coronal mass ejections (Antiochos 1998), coronal bright points (Golub et al. 1977), and ubiquitous coronal heating (Parker 1972). Of these, solar flares are the most often studied manifestation of reconnection. Many aspects typically observed in eruptive flares, such as separating flare ribbons, X-ray cusps, and posteruption downflows, have been attributed to consequences of reconnection in the scenario of Carmichael, Sturrock, Hirayama, Kopp, and Pneumann (CSHKP; see McKenzie 2002 for a review).

Due to their complex geometries, however, flares are poor contexts in which to study reconnection in detail. Reconnection is assumed to be responsible for the rapid energy release and possibly for energy dissipation, so the reconnection rate is presumed to be reflected in the intensity of flare emission. It has proven extremely difficult, however, to actually measure the *rate* of reconnection, defined as the rate at which field lines are topologically changed. The only studies that could qualify as such measurements have tracked the motions of chromospheric features, such as hard X-ray footpoints or flare ribbons (Fletcher & Hudson 2001). Since these signatures are considered to be magnetically linked to the reconnection site, it is argued, usually from the two-dimensional CSHKP picture, that the speed of apparent motion is related to the rate of reconnection.

Coronal loops connecting between two active regions offer some of the most compelling evidence of nonflaring reconnection in the solar corona (Sheeley et al. 1975; Tsuneta 1996; Pevtsov 2000). An active region is generally assumed to be produced by the buoyant emergence of one or more flux tubes from below the photosphere (see Fisher et al. 2000 and references therein for a review). Under this assumption, any coronal field interconnecting two distinct regions must have been produced through magnetic reconnection after emergence. The conclusion is particularly compelling when the loops interconnect active regions from opposite hemispheres.

In his pioneering study of reconnection between active regions, Tsuneta (1996) analyzed *Yohkoh* Soft X-Ray Telescope (SXT; Tsuneta et al. 1991) images of the bipolar NOAA active regions 7116 and 7117, which interacted across the equator between 1992 March 23 and April 2. Many of the SXT images show four distinct loop sets arranged in a symmetric X, resembling a magnetic X-point. Detailed analysis revealed that the interconnecting loop sets (east and west of the X), which had been presumably formed by reconnection at the X-point, were 2–3 times hotter than the loops internal to the active regions (4–7 MK vs. 2 MK). Tsuneta found that the post-reconnection flux would be heated sufficiently if all the energy of a 18–27 G upstream magnetic field were dissipated (converted to heat) as it passed the X-point at 1% of the upstream Alfvén speed. This reconnection seems to have progressed steadily, without explosive manifestations such as flares, and the magnetic structure of each active region changed continuously in accordance.

Tsuneta's study remains a valuable contribution to our present understanding of reconnection in the corona. The theoretical interpretation it proposes, Petschek reconnection at a magnetic neutral point, does present persistent difficulties. It is remarkable how clearly the SXT images, especially in the period around 1992 March 27, resemble the classic right-angle separatrices of a two-dimensional X-point. This is exactly the configuration we would expect if the magnetic field were current-free. Such a current-free field, however, would have no free energy to dissipate through reconnection. Furthermore, the brightest interconnecting loops are often very far from the X-point where they were supposedly energized. This separation is particularly puzzling in light of the rather short time, ~450 s, in which the author estimates the loops should conductively cool. Finally, it is not possible for a significant quantity of magnetic flux to pass through an isolated neutral point, or even through a neighborhood of that point. Three-dimensional reconnection models predict instead that reconnection must occur along a magnetic separator (Greene 1988; Lau & Finn 1990). The rate of reconnection will be given by the voltage difference between the

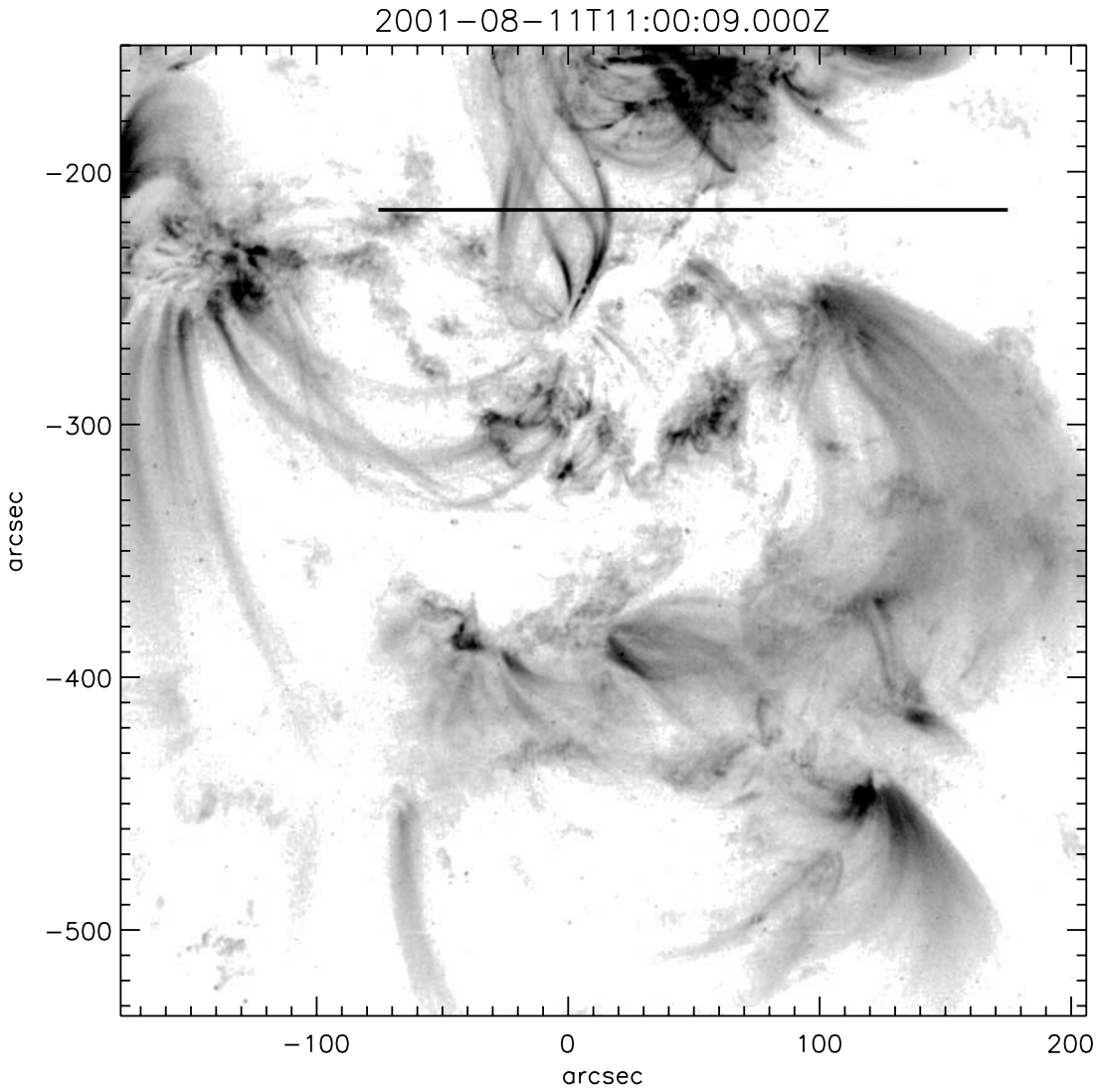

FIG. 1.—*TRACE* 171 Å image of AR 9570 and AR 9574 from 11:00 August 11, plotted as an inverse gray scale of the square root of the background-subtracted count rate. Axes are in arcseconds from disk center. The emerging active region, AR 9574, is partially cropped by the top of image; the older active region is located around $y = -250''$. The 600×3 pixel horizontal strip, centered at $y = -214\farcs7$, is shown as a dark horizontal line.

two ends of the separator field line (Sweet 1958; Longcope 1996).

The basic approach of studying nonexplosive reconnection between active regions, which Tsuneta (1996) pioneered, remains among the most promising avenues for quantifying reconnection and thereby illuminating its basic physical underpinnings. In this work we analyze data from the period 2001 August 10–11, during which active region 9574 emerged in the immediate vicinity of existing active region 9570. The emergence occurred as the pair crossed disk center and as the *Transition Region and Coronal Explorer* (*TRACE*; Handy et al. 1999) was making high-cadence observations of that area in the 171 Å passband.

The *TRACE* observations show numerous loops interconnecting the two regions and thereby provide an unprecedented opportunity to quantify magnetic reconnection. We herein use these observations to measure the reconnection rate, defined as the rate magnetic flux is topologically changed. We find that the reconnection rate is relatively small for the first ~24 hr of emergence and then rapidly increases to a peak as high as 10^{17} Mx s^{-1} (10^9 V). Comparison to a three-dimensional magnetic model reveals that the interconnecting loops are consistent with those produced by reconnection at a separator overlying the volume between the active regions. In this model the reconnection rate is the electromotive force (EMF) along the separator.

While the observations provide evidence that the interconnecting loops were formed by separator reconnection, they also suggest that the reconnection *did not* heat the loops significantly, at least not at the instant of reconnection. The prereconnection free magnetic energy predicted by the model is sufficient to provide all the heat ultimately observed. The long duration of the *TRACE* loops, in excess of their radiative cooling times, and their delayed appearance relative to soft X-ray loops observed by *Yohkoh* SXT suggest that the heat was instead deposited over many hours following the moment of reconnection.

The present work presents the data, measurements, and theoretical interpretation as separator reconnection in the following order. The next section presents the *TRACE* data set and describes the construction of a stack plot from it. Section 3 describes the magnetic data and its use in the production of a three-dimensional coronal model. Section 4 uses the stack plot and magnetic model to calculate the reconnection EMF. The magnetic model also predicts the free energy stored in the coronal field during the 24 hr delay between emergence and reconnection. Section 5 discusses

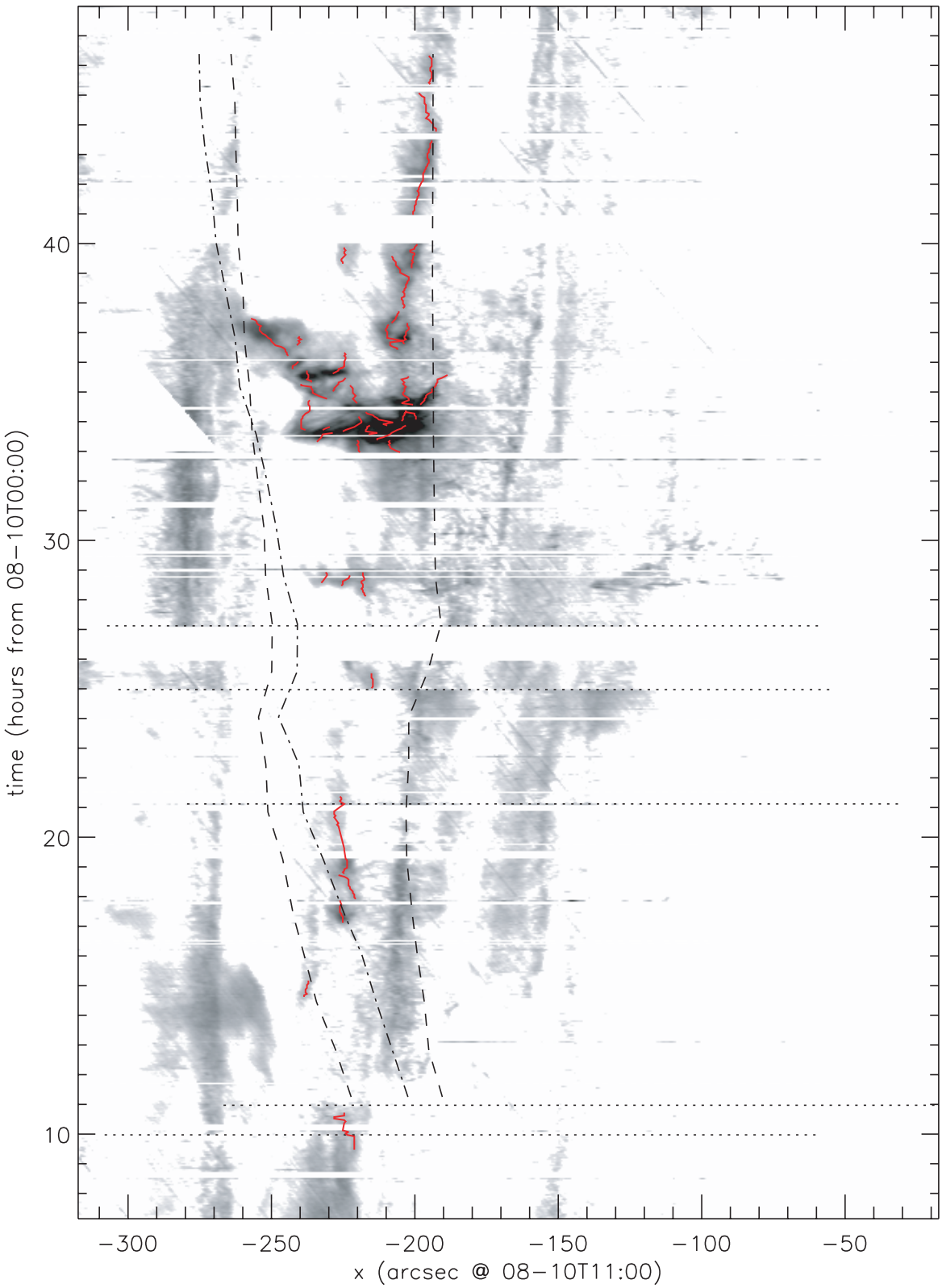

FIG. 2.—Stack plot from *TRACE* 171 Å within the horizontal slit. Inverse gray scale shows DN per second within the 3 pixel high strip between the active regions. The horizontal axis is the spatial coordinate, in arcseconds from disk center, rotated back to 11:00 August 10. The vertical coordinate is time in hours since 00:00 August 10. Dashed and dash-dotted lines are separatrices and separators from the magnetic model. Red solid curves indicate each of the loops identified in the stack plot and the images. The horizontal dotted lines denote the times at which the slit was moved vertically to accommodate the expansion of AR 9574.

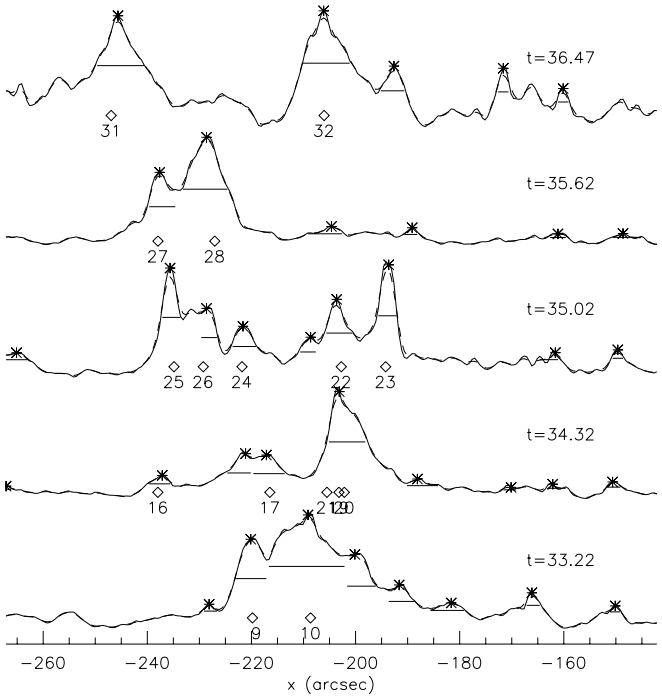

FIG. 3.—Five time slices from the stack plot in Fig. 2 from $t = 33.2$, 34.3, 35.0, 35.6, and 36.45 hr after 00:00 August 10 (i.e., from 9:12, 10:17, 11:00, 11:54, and 12:27 on August 11). Solid and dashed curves show the unsmoothed and smoothed intensities $I(x)$ and $\mathcal{SI}(x)$, respectively. Each curve is normalized to the global maximum of $I(x)$ for that time. Local maxima of $\mathcal{SI}$ are denoted by asterisks, and the pixels associated with that peak are indicated by a horizontal bar at the half-maximum level. Numbered diamonds are the peaks associated with legitimate coronal loops.

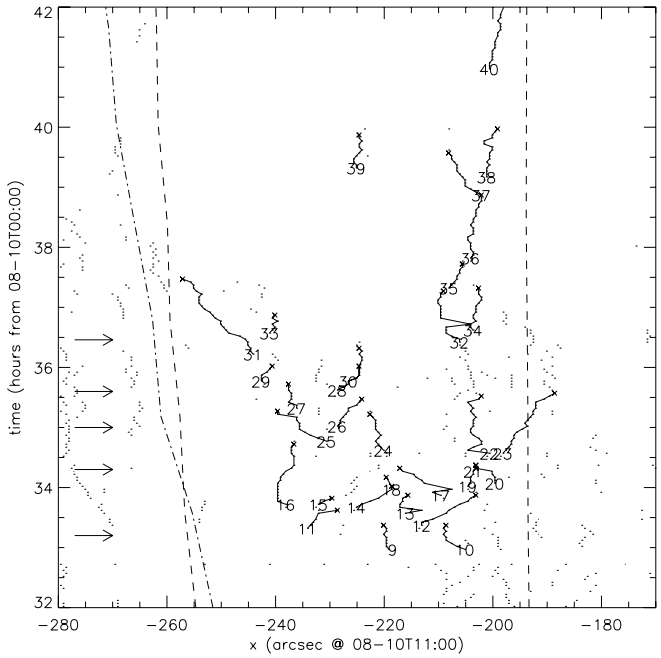

FIG. 4.—Peaks and loops from the stack plot. Dots indicate the peaks identified from maxima in time slices. Numbered curves are loops. Five arrows along the left indicate the times of the profiles shown in Fig. 3 and to panels 4–8 of Fig. 5.

the quantitative and qualitative implications of these observations. The last section presents a very brief synopsis of the observations and organizes them in terms of the magnetic model.

2. CORONAL OBSERVATIONS

The principal coronal data consist of 768×768 pixel 171 Å *TRACE* images made between 2001 August 10 7:00 and August 11 23:59 of the emerging active region 9574 and its neighbor AR 9570. (We chose not to use the 1600 Å, white-light, or 1024×1024 171 Å images that were made by *TRACE* at much lower cadence over this same period.) During this 41 hr interval 5139 images (768×768 pixels) were obtained, at an average cadence of one every 28 s (see Fig. 1). These were processed using standard software for flat-field correction, removal of cosmic-ray "spikes," and division by exposure time. After this, a uniform coronal background was subtracted (see Cirtain 2005 for details). Figure 1 is an example from 11:00 August 11 showing a portion of AR 9574 along the top, all of AR 9570, and several interconnecting loops.

In order to identify each and every interconnecting loop we define a horizontal line separating AR 9570 from AR 9574. The line is located 195″.7 south of disk center at 11:00 August 10 and is occasionally repositioned to accommodate the expansion of AR 9574. The line is shifted northward several times as AR 9574 is first emerging and then southward in steps of 5″ or 10″ as needed. After the final shift, at 4:00 on August 11, the line is located at $y = -215''.7$.

A synthetic slit consisting of a 600×3 strip of pixels lying along this line is extracted from each processed image (see Fig. 1). The slit is repositioned horizontally every hour or two to compensate crudely for solar rotation. The result, after averaging over the 3 pixel height of the strip, is a 600×5139 array of 171 Å intensity values. A final stack plot is then produced by averaging the slit-images into equal-time bins of $\Delta t = 3$ minutes. To compensate more precisely for solar rotation, the left pixel of each time bin is rotated to its position at 11:00 August 10. Figure 2 shows the resulting stack plot, along with the loops and elements of the magnetic model described below.

Each pixel of the stack plot results from two different averages. First there is a spatial average across the 3 pixel high slit, and then a temporal average over 3 minutes. As a result, the data in the stack plot have lower noise than the raw data. A histogram of pixels from a very dark section of Figure 2 has a width of $\sigma = 0.17$ DN s^{-1}. We take this as the noise level over the entire stack plot.

Interconnecting loops appear as slanted dark streaks in the stack plot (Fig. 2). Within a single intensity time slice, $I(x)$, a loop appears as a peak located where the loop crosses the slit. Intensity peaks are identified automatically by an algorithm that first locates local maxima in a smoothed curve, $\mathcal{SI}(x)$. The peak unsmoothed intensity must exceed 0.75 DN s^{-1}. Neighboring pixels are then assigned to that loop provided they are strictly downhill in the smoothed intensity $\mathcal{SI}(x)$ and also have an unsmoothed intensity $I(x)$ above one-half the peak's value. The downward extent from the peak must exceed 0.75 DN s^{-1} in at least one direction in order for the loop to be deemed distinct from its neighbors. Figure 3 shows the smoothed and unsmoothed curves, $\mathcal{SI}(x)$ and $I(x)$, at five different times. Peaks identified by the algorithm are denoted by asterisks, and the extent of the loop by a horizontal bar. These examples show several instances, such as one at the right of the top curve ($x \simeq -165$ for $t = 36.47$), where the peak has been deemed indistinguishable from neighboring peaks by the required 0.75 DN s^{-1}.

When the automatically identified peak locations are vertically stacked, as in Figure 4, genuine loops stand out in tilted rows while spurious peaks appear as isolated dots. Each row of three more points falling on a roughly straight line was manually

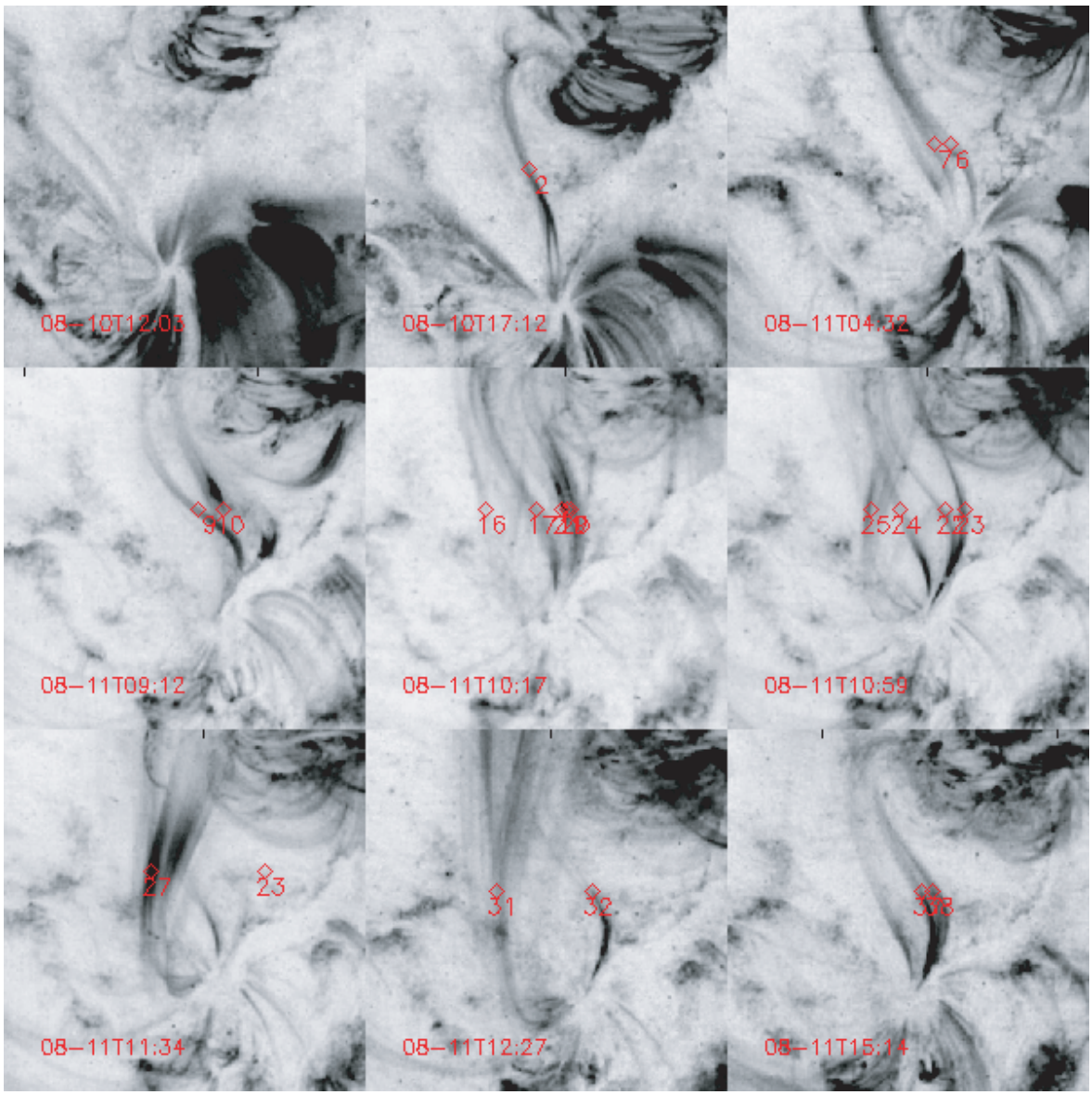

FIG. 5.—Composite of interconnecting loops from the emergence of AR 9574. Nine selected times read chronologically from left to right, top to bottom; times are indicated in the lower left of each image. Diamonds are the identified loops. Panels 4–8 correspond to profiles in Fig. 3.

selected from such a plot and designated as a loop. A continuous row of points with an abrupt direction change (i.e., change in apparent velocity) was considered to be two distinct loops, such as loops 36 and 37 in Figure 4. After all rows of points were selected, their locations were then overplotted on a spatial image as shown in Figure 5. Identifications that appeared to be something other than a loop or that appeared to be non-interconnecting loops crossing the slit were eliminated from the loop list. There are several instances where a row of vertical (stationary) points correspond to generalized low-altitude brightenings such as "moss" (Berger et al. 1999).

The final result of this procedure was a complete list of 43 interconnecting loops that we number 0–42 in order of appearance. The very fist loop, loop 0 at 9:27 August 10, is the earliest hint in 171 Å of a connection between active regions. Prior to this the leading pole of AR 9570 has numerous radial loops fanning out like spokes, producing the enhancement at $x \simeq -230$ of the stack plot (Fig. 2). At 9:27 one spoke appears to be aimed toward the emerging active region, and we take this as the first interconnection, loop 0, even though its northern footpoint is invisible. The second loop, loop 1, appears at 14:36 and is unambiguously an interconnecting loop. All subsequent loops, such as loop 2 shown in Figure 5, have the same unmistakable interconnecting form.

Each of the 43 loops is characterized by parameters found from the stack plot. Loop 1, for example, remains bright in 171 Å for 36 minutes, in the sense that its peak is identifiable as described above. Its diameter is 1.8 Mm, found from the median over all times of the FWHM at each time. The crossing point moves westward at an average speed of 543 m s^{-1}, resulting in a right-tending streak on the stack plot (Fig. 2). The streak is 1.12 DN s^{-1} in its brightest pixel, but has a mean intensity of $I = 0.79$ DN s^{-1} over its 36 minute duration.

Loop 1 turns out to be among the faintest of the entire set, perhaps because it is the first genuine interconnection. Although its peak intensity is small (1.12 DN s^{-1}), it is well above the noise floor, which we earlier estimated to be $\sigma = 0.17$ DN s^{-1}. Subsequent loops have peaks in the range 1.5–5 DN s^{-1}, until

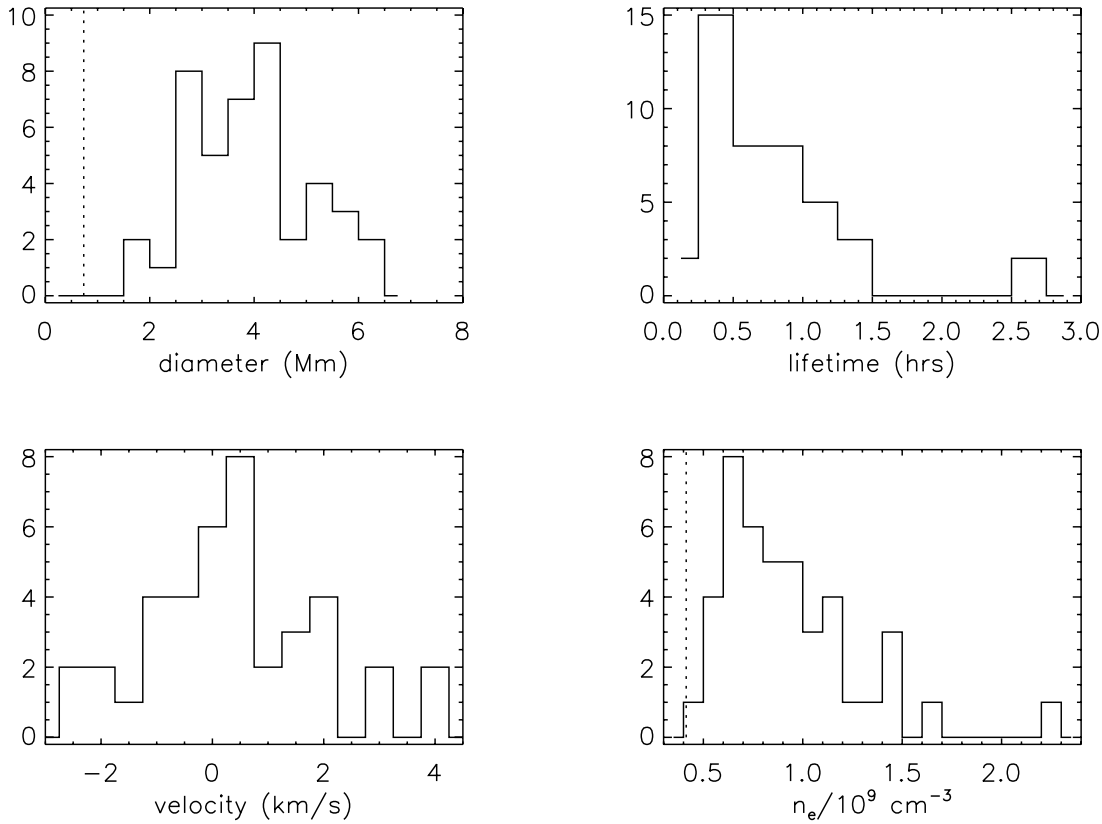

FIG. 6.—Histograms summarizing properties of the 43 loops interconnecting AR 9570 and AR 9574. A vertical dotted line marks the Nyquist limit, 2 pixels, on the diameter plot. The vertical dotted line on the density histogram is the density of a loop at the detection threshold of 0.75 DN s^{-1} whose diameter is the typical value of 4 Mm.

loops 10–23 starting at 8:57 on August 11, which have peak emissions in the range 10–40 DN s^{-1}. Thereafter loop peak intensities return back to a level of 1–10 DN s^{-1}. We return below to discuss the significance of the period of brighter interconnecting loops.

The intensity I of a loop puts a lower bound on its electron density. The response of the *TRACE* 171 Å imager reaches a maximum, $R_{\max} = 1.1 \times 10^{-26}$ DN s^{-1} cm^5 in a single pixel, at a temperature of $T_e = 0.95 \times 10^6$ K (Aschwanden et al. 2000). Assuming the loop to be uniformly filled across its diameter, d, with plasma at the optimal temperature provides a lower bound on the electron density of the loop

$$n_e = \sqrt{\frac{I}{R_{\max} d}}. \quad (1)$$

The density bound for loop 1 is $n_e = 6.3 \times 10^8$ cm^{-3} using its mean intensity, but is no less than $n_e = 7.5 \times 10^8$ cm^{-3} at the instant of peak emission.

The values found for all 43 loops are summarized in the histograms in Figure 6. From these it appears that loops are typically ~3.7 Mm (the median of all medians), which move across the slit at around 1 km s^{-1}. The density histogram in Figure 6 shows the lower bound from the mean intensity value of each loop, as defined by equation (1). The majority of loops have values of $(0.5–1.0) \times 10^9$ cm^{-3} for this lower bound. For 4 Mm diameter loops, typical of the ones observed, the detection threshold of 0.75 DN s^{-1} corresponds to an average electron density of $n_e = 0.4 \times 10^9$ cm^{-3}; this is taken as the detection limit in our analysis.

Of the total background-subtracted EUV intensity along the slit, most comes from the interconnecting loops that we have identified. The dashed lines in stack plot Figure 2 are from a magnetic model explained below. It is evident that they encompass, for the most part, that segment of the slit where interconnecting loops occur. Integrating the emission across this segment and out to 20″ beyond it gives the dashed line in Figure 7, which we consider the total EUV emission. The solid curve is the corresponding emission from only those pixels in the identified loops. This can be seen to be a significant fraction of the total. In some cases the total intensity is actually *less* than that part in identified loops. This occurs due to negative contributions from the surrounding regions, resulting from background subtraction. Although at most times the loop-attributed intensity is the majority of the total intensity, obvious exceptions occur at $t = 25$ and $t = 32$. These are found, by examination of the stack plot Figure 2 and corresponding spatial images, to result from general brightenings of diffuse emission such as moss. This appears in the $t = 33.0$ time slice, the bottom curve in Figure 3, as broad emission between $x = -210$ and -190.

3. THE MAGNETIC MODEL

3.1. *The Magnetic Data*

Magnetic data of the active region's emergence is provided by full-disk magnetograms made every 96 minutes by the Michelson Doppler Imager (MDI) on board the *Solar and Heliospheric Observatory* (Scherrer et al. 1995). A subregion was extracted from each full-disk magnetogram, and the measured values were multiplied by the calibration factor 1.56 following Berger & Lites (2003). Polarity concentrations were automatically identified by locating local maxima in a smoothed magnetogram and associating with each maximum all surrounding pixels that are both downhill in the smoothed magnetogram and have values of $B_{\rm los}$

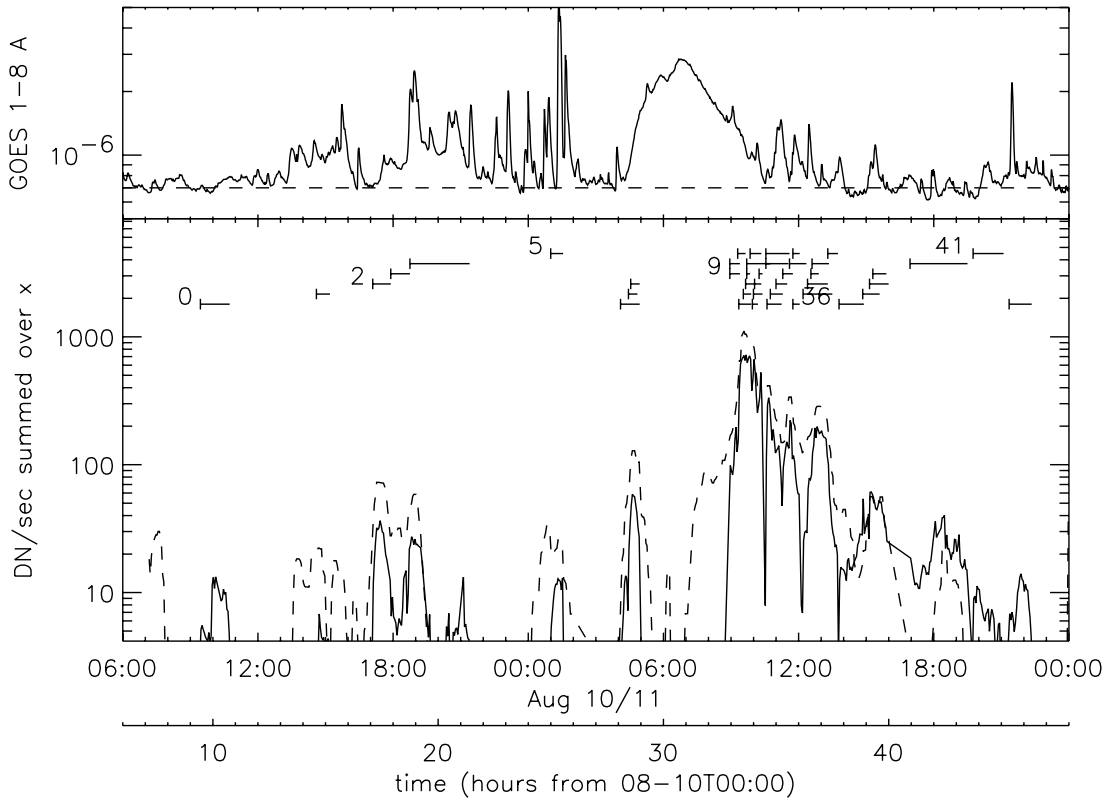

FIG. 7.—Time histories of the emissions from reconnected flux. The bottom panel shows the integrated 171 Å emission from loops (*solid curve*) and from all pixels within the interconnecting region (*dashed curve*). Horizontal bars across the top show the lives of each of the identified loops, several of which are numbered. For convenience, time axes are given for both hours after 00:00 August 10 and in conventional 24 hr notation. The top panel shows the *GOES* 1–8 Å channel, in W m^{-2}, for reference. The dashed line is 0.7×10^{-6} W m^{-2}, the approximate background level at this time.

above 45 G. Regions with fewer than 40 pixels were then discarded. Examples of the raw magnetograms and identified concentrations are shown in Figure 8.

A magnetic model of the active region complex was constructed from the identified polarity concentrations. The flux of each concentration is found by summing the pixels from line-of-sight measurement and increasing them by a factor under the assumption that the field is purely radial at the photosphere. There is a small but persistent imbalance between opposing polarities, even within the emerging active region. We do expect the more concentrated leading (negative) polarity to be favored by our thresholding procedure and possibly by the response of MDI (Berger & Lites 2003). To compensate for this we augment the fluxes in positive concentration by 7.5%. This seems to restore approximate flux balance to both active regions at the same time.

The corrected flux from each concentration is then assigned to a point charge located at the concentration's center of flux. This charge is then projected onto a tangent plane whose point of tangency is near the center of unsigned flux (the exact point is at 9°.15 south, rotates at 13°.5 per day, and crosses the central meridian at 15:41 on August 11).

The leading polarity and only sunspot in the older active region, AR 9570, is the largest concentration N01, which does not move appreciably over the entire period. The following polarity consists of numerous small positive concentrations that move about in a complex manner, occasionally appearing or disappearing; this does not, however, appear to correspond to any systematic motion. The emerging active region, AR 9574, consists of two positive concentrations, P18 and P051, and two negative concentrations, N07 and N30. These grow and separate during most of the observation. The flux-weighted midpoint of each polarity separates at an approximately constant rate of 215 m s^{-1} along a line 8°.4 south of west.

The largest flux concentrations include sunspots and very strong fields, to which MDI is known to be less sensitive. Our calculations will therefore underestimate the fluxes of the largest concentrations. There seems to be no accepted method for correcting this instrumental artifact, but it is possible to estimate its magnitude. Berger & Lites (2003) observe a weakened MDI response when the vertical field strength exceeds $B_{\rm sat} = 1700$ G, and their calibration factor of 1.56 fits the instrument's response to fields weaker than this value. Using this same factor in strong field regions, as we have done, will undercount total fluxes there. The amount of undercounting can be estimated by integrating $|B_{\rm los}| - B_{\rm sat}$ over all pixels whose adjusted strength exceeds $B_{\rm sat}$. This integral is 4.1% and 4.5% of the total fluxes in regions N01 and P051 at the late time 17:39 on August 11 (P18, N07, and N30 have values between 0.7% and 1.7% of their total fluxes). If the sensitivity of MDI to fields stronger than $B_{\rm sat}$ were actually reduced by exactly one-half, then these small factors would be the relative undercounting of the fluxes in each region. Plots in Berger & Lites (2003) indicate that the sensitivity is probably not reduced quite that much, nor is the response really piecewise linear. Thus we retain the values calculated with the uniform correction factor of 1.56 and bear in mind that the two largest sources, N01 and P051, are in reality larger than they are in our model, but probably by no more than a few percent.

The evolution of fluxes in the various concentrations is summarized in Figure 9. The three solid lines are the net flux in the positive polarity (*top line*), negative polarity (*bottom line*), and entirety of AR 9574 (net signed flux; *middle line*). The three

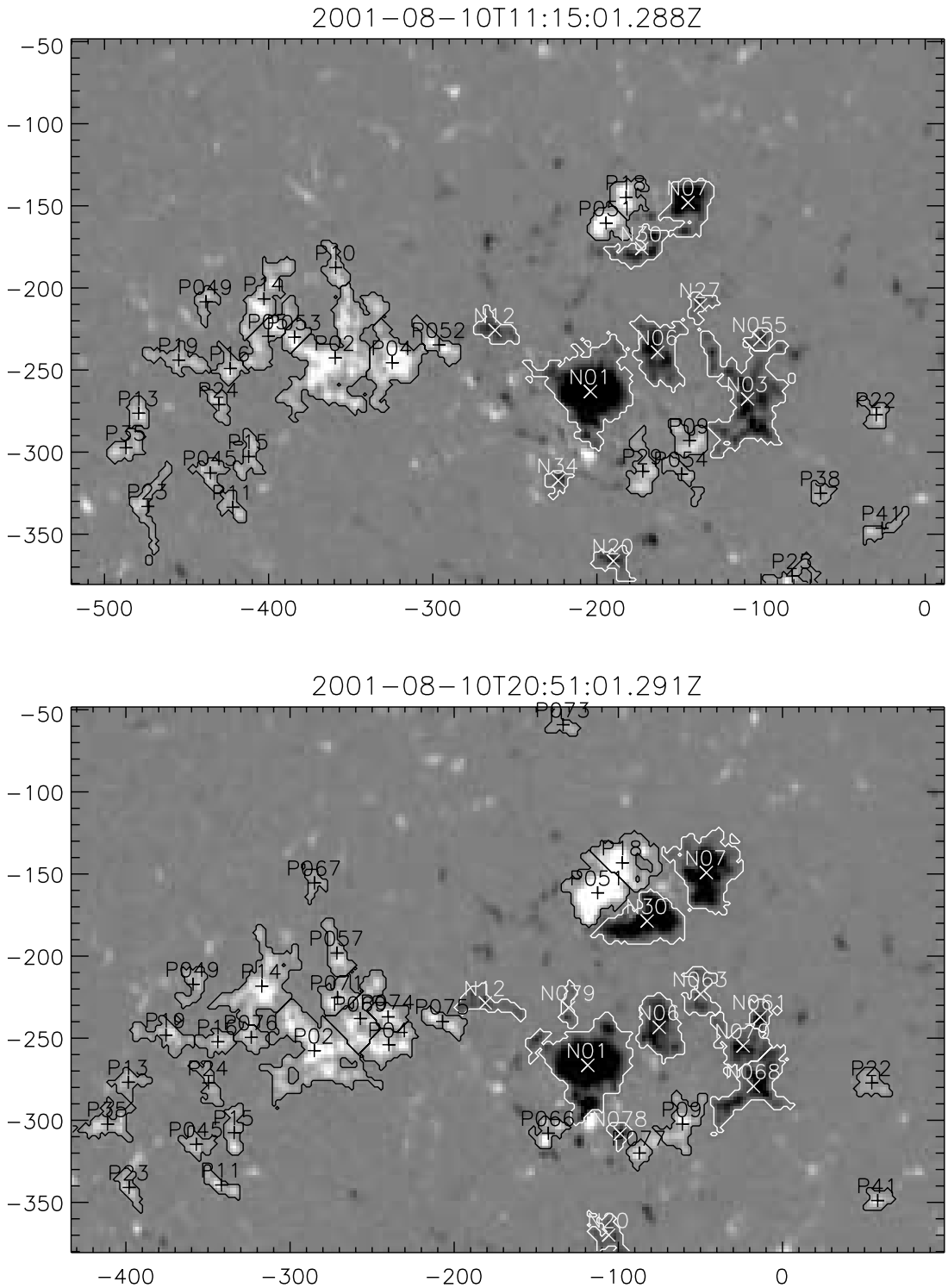

FIG. 8.—Magnetograms of AR 9570 and AR 9574 at 11:15 (*top*) and 20:51 (*bottom*) on August 10. Gray scale shows the line-of-sight field strength between ±500 G (after applying a calibration factor of 1.56). Each identified concentration above 45 G is traced out. A plus sign (+) or cross (×) marks the center of flux in a positive or negative region, with the region's name just above.

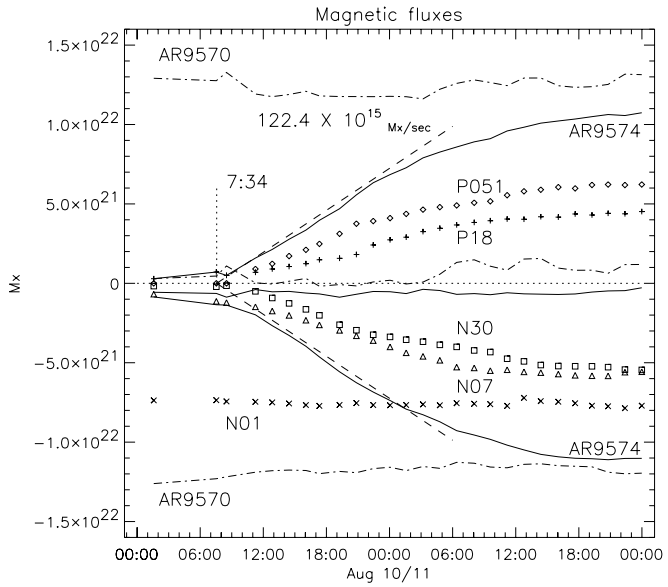

FIG. 9.—Evolution of flux in AR 9574 (*solid lines*) and AR 9570 (*dash-dotted lines*) and several specific concentrations (*symbols*). The top and bottom line of each type are the total flux in positive and negative polarities, respectively. The center line, hovering near zero, is the net signed flux in each active region.

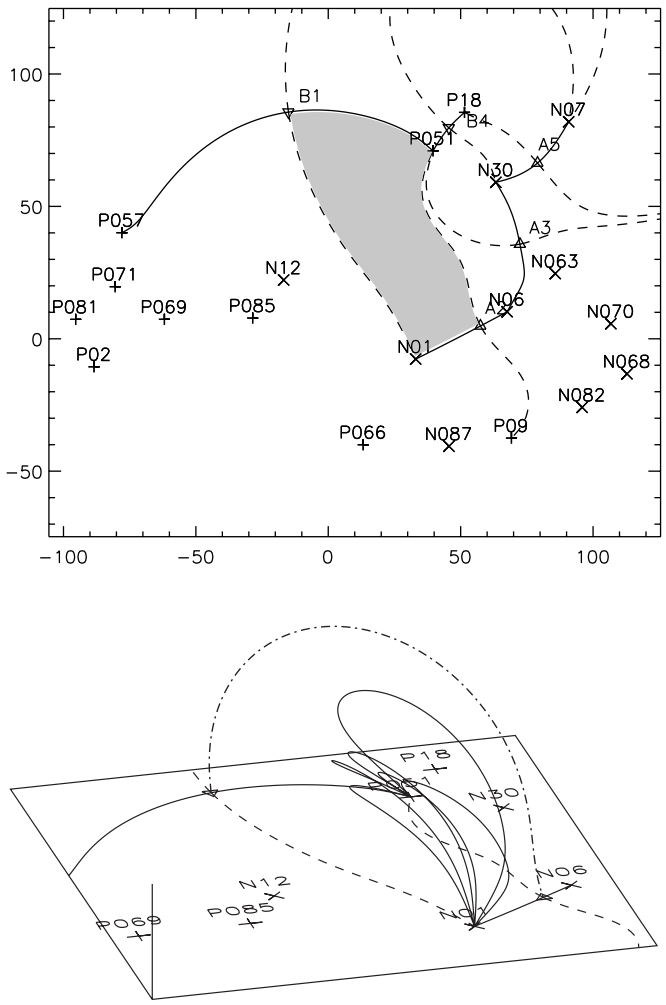

FIG. 10.—Potential magnetic field model at 22:27 on August 10. *Top*: Footprint of the skeleton showing locations of positive and negative sources as plus signs (+) and crosses (×), respectively. Five null points, labeled B1–A5, are designated by triangles (△ and ▽ for negative [B] and positive [A] null points). Dashed curves are the photospheric portion of the fans, and solid lines are the spines. The shaded region is the footprint of domain P051–N01. *Bottom*: Perspective view of field lines belonging to domain P051–N01 (*thin solid curves*). The thick dash-dotted line is the separator linking null points B1–A2.

dash-dotted lines give the same values for AR 9570. The middle lines show the extent to which the 7.5% correction has restored flux balance to each of the active regions. The flux in the older region, AR 9570, remains approximately constant, $\sim 1.2 \times 10^{22}$ Mx, while that in the emerging region increases beginning at ~7:34 August 10. Even though some flux concentrations exist prior to 00:00 August 10, the emergence appears to begin in earnest only after 7:00. During the initial phase the flux in each polarity increases at approximately 122.4×10^{15} Mx s^{-1}, shown by dashed lines. This linear fit intersects zero at 7:34, which we take to be the initiation of genuine flux emergence. Prior to this the flux in AR 9574 is poorly organized and does not increase very rapidly.

3.2. *The Model*

The observations are used in a magnetic model for the effect of active region emergence. The dispersed nature of the following polarity of AR 9570 results in appearance and disappearance of identified concentrations, partly as an artifact of the thresholding and other processing steps. In order to focus on the emergence rather than these other, partly artificial effects, we freeze AR 9570 in the configuration from 17:20 on August 10. This configuration consists of 32 concentrations, 10 negative and 22 positive, that represent the dispersed following plage. Each source is reduced to a total flux and centroid location on the tangent plane. The configuration is "frozen" in the sense that the fluxes remain constant and locations are fixed to the tangent plane, which itself rotates with the Sun. The four concentrations of AR 9574, designated P18, P051, N07, and N30, vary in time according to the magnetograms. These four time-varying sources are added to the 32 sources from AR 9570 to produce the complete magnetic model.

The simplest model of the coronal field is a potential field extrapolated from the 36 point sources situated on the $z = 0$ plane. Source region i, with net flux Φ_i, is modeled by a point source with magnetic charge $q_i = \Phi_i/2\pi$. Placing all sources on the same tangent plane guarantees that all flux from the upward-facing hemisphere of each charge enters the corona. The resulting potential field has 37 photospheric null points (also in the $z = 0$ plane), including one with a vertical spine, known as an *upright* null. The field lines in this model fall into 105 domains, according to which negative and positive sources they interconnect (Longcope 1996, 2001). Mapping fan and spine field lines from each of the null points produces a *skeleton* of the potential field (Bungey et al. 1996; Longcope & Klapper 2002), dividing it into its 105 domains. Figure 10 (*top*) shows the footprint of the skeleton in the vicinity of the emerging active region. The dashed and solid curves, originating from each of five selected null points, divide the plane into six regions that are the footprints of six domains. One domain near the center consists of field lines connecting positive source P051 (one of the following sunspots in AR 9574) to negative source N01 (the leading sunspot of AR 9570). This domain is bounded by spines and fans from null points labeled B1 and A2, and shaded in Figure 10 (*top*).

In this potential-field model, source P18 (the northern positive sunspot in the emerging region) connects only to the negative sources in the same region (namely N07 and N30). The other positive source, P051, connects to these and also to N01 and N06 in the other active region. The negative sources in the

emerging region connect via long arching field lines to numerous small sources in the following plage of AR 9570. Of these interconnecting domains we focus on P051–N01 since it is by far the largest and appears to be the domain of the observed loops. Figure 10 (*bottom*) shows a perspective view of some representative field lines from this domain.

Domain P051–N01 is enclosed by the fan surfaces of null points B1 and A2. This the shaded region of the footprint of the potential field (Fig. 10, *top*), where the domain is bounded by fan traces (*dashed curves*) and spine field lines (*solid curves*) from each null. This structure is, however, topologically robust and will persist in any nonpotential field in which the domain P051–N01 is present. In all such fields the fans extend upward into the corona, forming a tent above the domain. The tent's ridgeline is formed by the separator where the two fan surfaces intersect. In the potential field the separator is the single field line running from null point B1 to null point A2.

Because of its location at the ridge of the enclosing tent, the separator encloses all field lines from domain P051 to N01, and no others. A curve within the separator, directed from B1 to A2, may be closed along the photosphere to form a circuit $\mathcal{Q}$. (It must be recalled that while the separator of a potential field is a single field line, in a general field it may be a ribbon of field lines [Longcope & Cowley 1996].) Integrating the vector potential $\boldsymbol{A}$ along this circuit gives the total flux interconnecting sources P051 and N01 (Longcope 1996; Longcope & Klapper 2002)

$$\psi = \int_{\mathcal{S}} \boldsymbol{B} \cdot d\boldsymbol{a} = \oint_{\mathcal{Q}} \boldsymbol{A} \cdot d\boldsymbol{l}, \tag{2}$$

where $\mathcal{S}$ is some surface bounded by $\mathcal{Q}$. Performing this integral for the *potential* field generated from the point-source model of the MDI magnetograms yields a flux $\psi^{(v)}(t)$ as a function of time. This time-dependent function, plotted in Figure 11, is negative since the field lines pass under the separator in the negative sense: following the separator from B1 to A2 with the fingers of the left hand, the field is directed along the thumb, toward the south. Throughout the emergence process, approximately one-third of the flux from P051 connects to N01 in the potential field; most of the rest remains within AR 9574, connecting to N07 or N30.

While the actual coronal field may differ from the potential model, it will nevertheless have a separator from which an isolating loop $\mathcal{Q}$ may be constructed. As in the potential model, all interconnecting flux must pass through $\mathcal{Q}$, and expression (2) will yield the total interconnecting flux. The amount of interconnecting flux can change only if a loop voltage

$$\frac{d\psi}{dt} = -\oint_{\mathcal{Q}} \boldsymbol{E} \cdot d\boldsymbol{l} \tag{3}$$

is produced along the circuit $\mathcal{Q}$. In principle there could be a contribution to equation (3) from an electric field along the photospheric leg of $\mathcal{Q}$. This contribution would arise from $\boldsymbol{v} \times \boldsymbol{B}$ as flux crosses the photosphere corresponding to the emergence of field lines already interconnecting the different active regions. Since the positive and negative poles of AR 9574 increase together, it seems likely that all emerging flux takes the form of a classic flux tube interconnecting the region's two polarities. For this reason we reject the possibility and thereby assume that the full voltage drop occurs along the coronal separator.

Rejecting the possibility that interconnecting field lines were created through emergence leaves only the possibility of separator reconnection manifest as a parallel electric field along the separator. As the potential field evolves it undergoes kinematic reconnection across the separator (Greene 1988; Lau & Finn 1990). In this reconnection, field lines from domain P057 to N01 of AR 9570 and field lines from P051 to N06 approach the separator. Field lines from each domain meet at the separator, break, and are rejoined with swapped ends to form new field lines in domains P051–N01 and P057–N06. It is the former field lines that augment the flux in the interconnecting domain. The theory requires that for each such field line added to P051–N01, one must also be added to P057–N06. Reconnection in the actual coronal field must be topologically equivalent to this, although the separator may be deformed into a ribbon of finite width (Longcope & Cowley 1996).

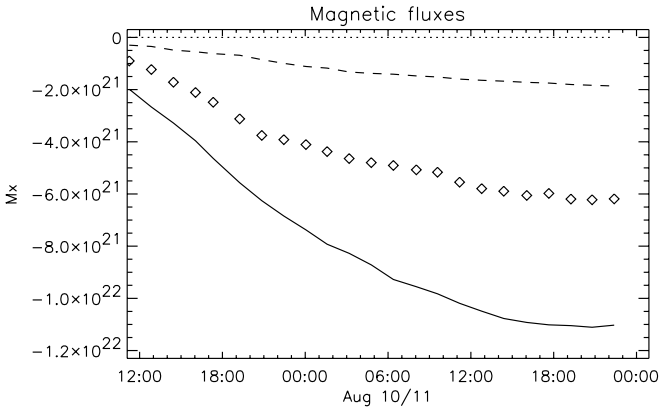

FIG. 11.—Total flux connecting P051 to N01, $\psi^{(v)}(t)$ (*dashed line*). The solid line is the total flux in the negative polarity of AR 9574, as shown in Fig. 9. The diamonds are the negative of the flux in source P051.

Our analysis replaces each of the observed flux concentrations with a magnetic point source. A point source located at the centroid (and within the $z = 0$ plane) is the leading term in a multipole expansion of the potential field from the extended source region. The use of point sources, while convenient, is not essential for the topological analysis. The same topology described above would be found if the photospheric field were extrapolated directly from the extended source regions (Longcope 2001). Separatrices, for example, are surfaces separating field lines with distinct footpoint locations. As long as the photospheric field consists of distinguishable regions, the coronal field will have separatrices. The crucial step in establishing a topology is, therefore, the division of the photosphere into distinct regions, in particular the separation of flux belonging to AR 9574 from that belonging to AR 9570. As long as such a separation is possible there will be separatrices, a separator, and the possibility of separator reconnection, exactly as described above.

4. QUANTIFYING THE RECONNECTION

The *TRACE* data presented in § 2 provide clear observational evidence of flux in the P051–N01 domain, which, as the previous section argued, must result from separator reconnection. To quantify this reconnection we will use the observations to estimate the total amount of interconnecting flux. Doing so requires four basic assumptions, which we number as an aid to future discussion. (1) We assume that each of the 43 identified loops is a bundle of field lines, also called a flux tube, from domain P051–N01. (2) We assume that the loops, and therefore also the flux tubes, have circular cross sections whose diameters are the FWHM found in the 171 Å images. (3) We assume that over its observed duration a given coronal loop tracks a single

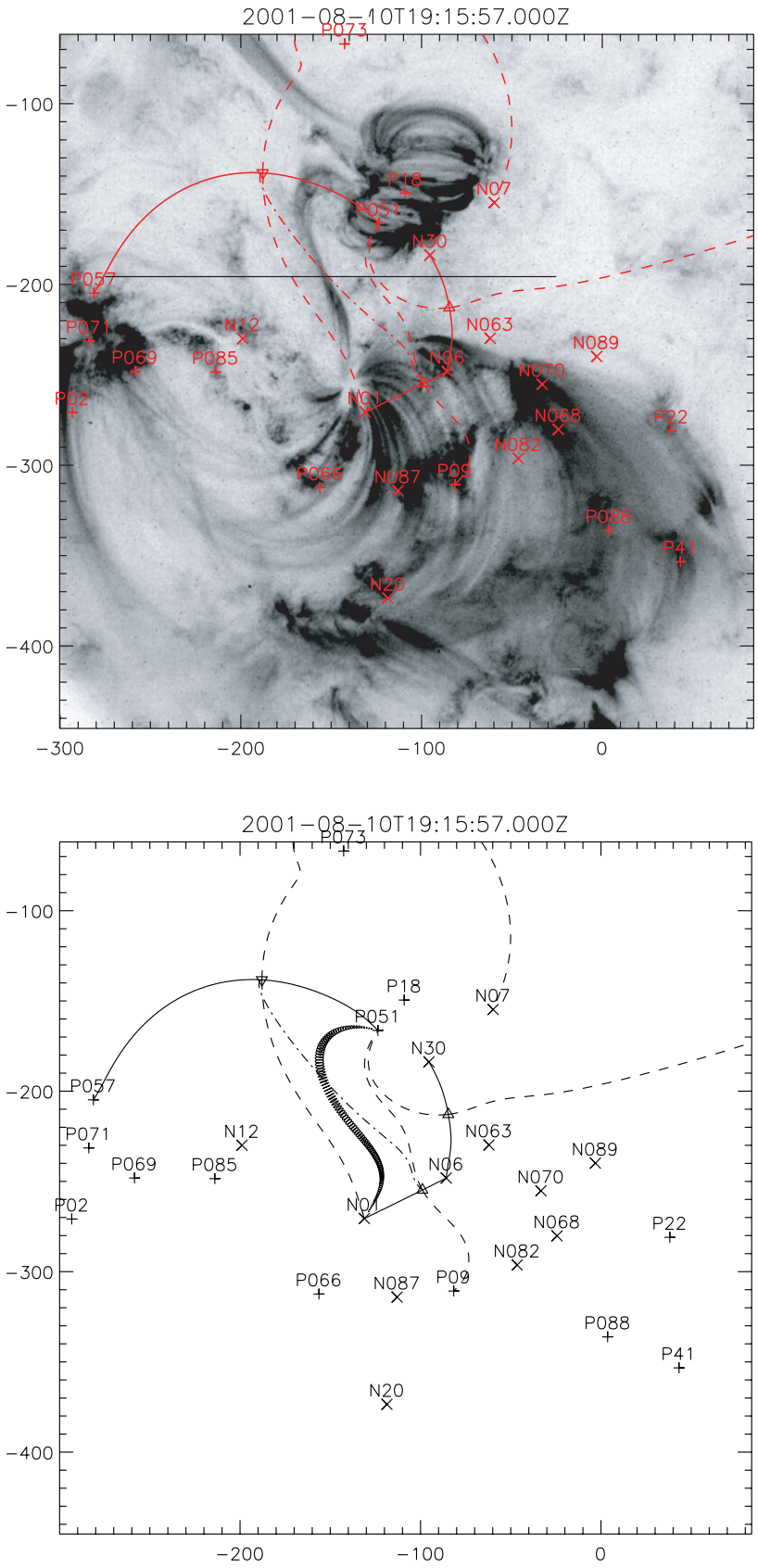

FIG. 12.— Correspondence between an identified coronal loop (loop 4) observed at August 10 19:15, and a field line from domain P051–N01 in the magnetic model from the same time. *Top*: Superposition of the *TRACE* image (*gray scale*) and the footprint of the field (*red lines*). The black horizontal line is the slit at that time. *Bottom*: Footprint and a flux tube from domain P051–N01 (*dark curved feature*).

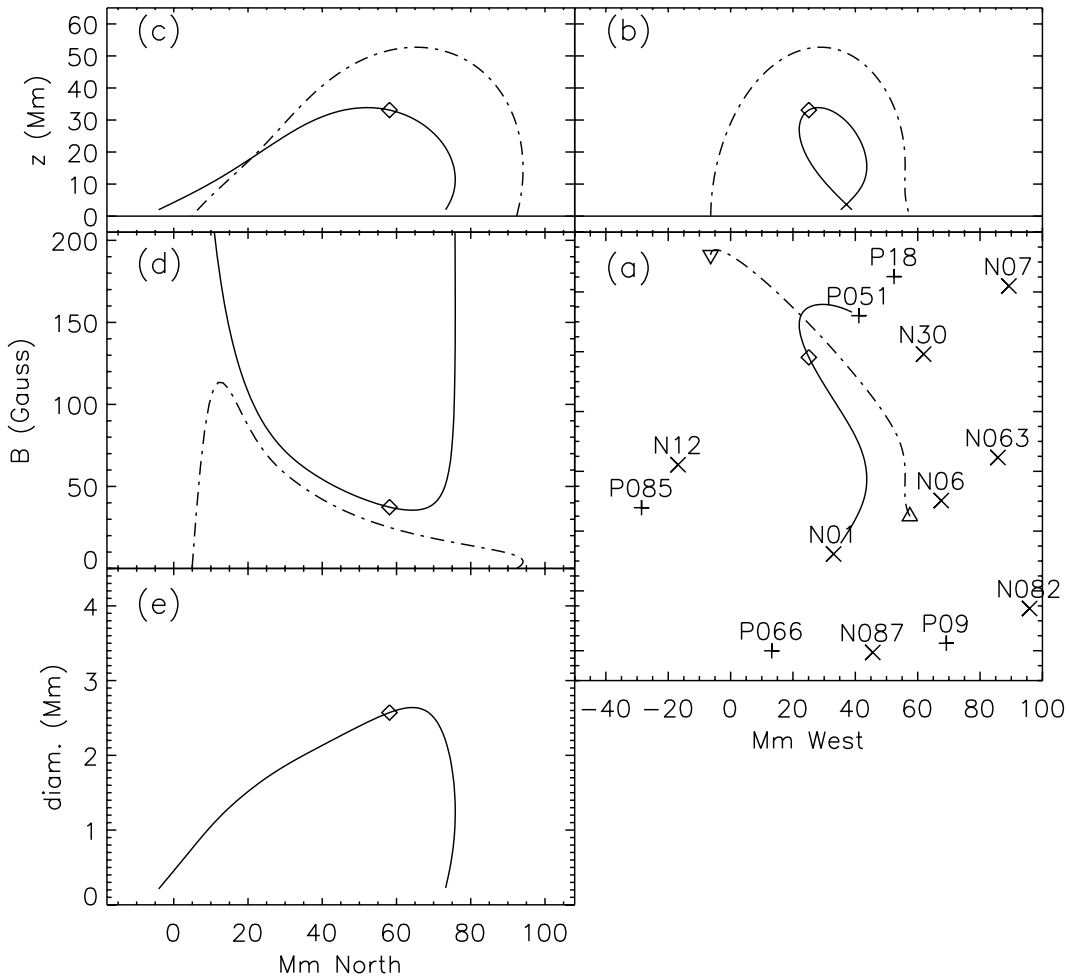

FIG. 13.—Field line selected to model loop 4 at 19:00 on August 10. Each panel shows the field line (*solid line*), the separator (*dash-dotted line*), and the point of slit-crossing (*diamond*). The different plots are, reading counterclockwise from lower right, (*a*) a view from above the tangent plane showing the neighboring sources; elevations as seen from a viewpoint (*b*) to the south and (*c*) to the east; plots of the loop properties as a function of the *y*-coordinate showing (*d*) the magnetic field strength and (*e*) the flux tube diameter.

flux tube. (4) We assume that no flux tube reappears in 171 Å, and thus that every identified loop represents a different interconnecting flux tube.

The assumed correspondence between observed coronal loops and model flux tubes is illustrated by Figure 12. The *TRACE* image shows a particular loop (loop 4) crossing the slit (*solid horizontal line*) and the footprint of the model field (*red lines*). The first point worthy of note is that the fan surfaces of both B1 and A2 (*dashed lines*) cross the slit and that the coronal loop crosses between them. The time evolution of the potential-field fan surface crossing points is plotted as dashed curves in the stack plots shown in Figures 2 and 4. As the domain flux, $\psi^{(v)}$, grows, the separatrices expand, causing the crossing points to separate. Almost all observed loops, when projected along the line of sight, fall between the separatrices of the potential-field domain P051–N01, giving credence to assumption 1: loops appear to be associated with field lines in the P051–N01 domain.

A flux tube in domain P051–N01 is selected to resemble loop 4. To do this, model field lines are integrated from various points along the line of sight defined by the intersection of loop 4 and the slit. One starting from a height of $z = 33$ Mm is selected due to its resemblance to the overall shape of the loop (see Fig. 12, *bottom*). The characteristics of this field line and of the separator are summarized in Figure 13. At the slit-crossing point (*diamond*) the field line has strength $|\boldsymbol{B}| = 37$ G and loop number 4 has diameter (FWHM) $d = 2.6$ Mm (Figs. 13*d* and 13*e*, respectively). A circular flux tube with this diameter encloses a total flux $\Phi = 2.0 \times 10^{18}$ Mx.

More generally, a field strength B_0 at the slit crossing implies that a tube whose apparent diameter is d has flux $\Phi = (\pi/4)d^2 B_0$. The 43 observed loops have a median diameter $d = 3.7$ Mm, corresponding to a flux $\Phi = 4 \times 10^{18}$ Mx if the field strength were $B_0 = 37$ G, as it is for the potential-field model of loop 4. The fact that all of the reconnected flux seen at 171 Å takes the form of loops with very similar diameters suggests a sporadic or patchy reconnection transferring flux in parcels of $\sim 4 \times 10^{18}$ Mx at a time.

The total flux transferred by all 43 flux tubes will be $\Delta\psi \simeq 43\Phi = 1.7 \times 10^{20}$ Mx. Accumulating the cross-sectional area of the actual loops and attributing each to the time of its first appearance generates the area curve $A(t)$ shown in Figure 14. The curve jumps by $(\pi/4)d^2$ at the onset of each loop brightening. The duration of that loop is indicated by a horizontal line beginning at the jump. The curve rises quite gradually until 9:00 August 11, when a flurry of loop brightenings causes it to rise at $\dot{A} \simeq 3.9 \times 10^{14}$ cm^2 s^{-1} for a 3 hr interval.

The flurry of brightenings persists for approximately 3.5 hr, transferring $\sim 2 \times 10^{19}$ cm^2 of accumulated area. The plot in Figure 14 uses a less conservative field strength of $B_0 \simeq 120$ G, since it is the largest value we consider plausible, makes the

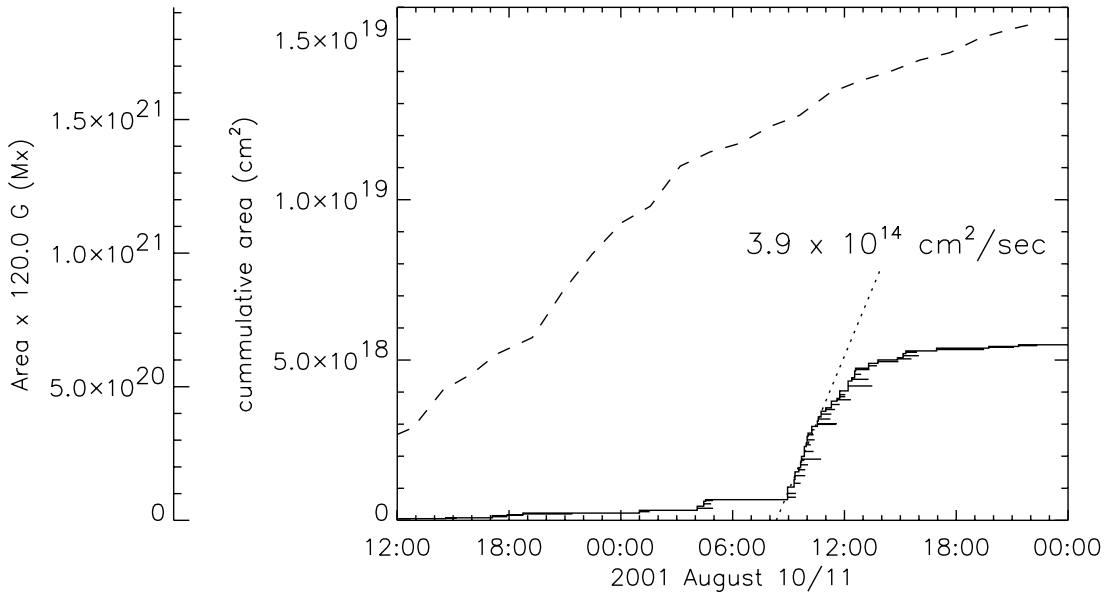

FIG. 14.—Accumulated areas of coronal loops $A(t)$ (*solid curve*). The curve jumps by $(\pi/4)d^2$ at the initiation of each loop. A horizontal bar from that point indicates the duration of that loop. A second axis gives the equivalent flux assuming a field strength of $B_0 = 120$ G. The dashed curve shows the interconnecting flux in a potential model, $\psi^{(v)}(t)$, on the flux axis.

plot clearer, and helps illustrate further discussion. With this larger value, $\Delta\psi \simeq 5 \times 10^{20}$ Mx of flux is transferred in 3.5 hr (the minimum possible value, $B_0 = 37$ G, gives only one-third this much). These observed flux transfers can be compared to the potential field values $\psi^{(v)}(t)$ (*dashed line*), whereby $\simeq 1.5 \times 10^{21}$ Mx is transferred steadily over 36 hr at an average rate of 11.6×10^{15} Mx s^{-1}. The observed loops account for between one-ninth and one-third of this transfer rate, depending on B_0, the assumed field strength in the tubes. The peak transfer rate exceeds the average rate at which a potential field would transfer flux by as much as a factor of 3.

The loop observations can also be used to quantify the energy input into the plasma. The density lower bound n_e puts a lower bound on radiative power density

$$\mathcal{P}_r = \alpha_{\rm Fe} n_e^2 \Lambda_0, \tag{4}$$

where $\alpha_{\rm Fe}$ parameterizes the relative abundance of iron and the radiative loss function has been approximated as $\Lambda(T_e) \simeq \Lambda_0 = 10^{-21.94}$ ergs s^{-1} cm^3, a constant over the peak *TRACE* response 0.5 MK $< T_e <$ 2.0 MK (Rosner et al. 1978; Aschwanden et al. 2003). The radiative power density defines a radiative cooling time $\tau_{\rm rad} \equiv 3 n_e k_{\rm B} T_e / \mathcal{P}_r$, which will be an upper bound on the expected lifetime of a freely cooling loop since our density estimates are themselves lower bounds. The 171 Å response has half its peak value within the range 0.65 MK $< T_e <$ 1.25 MK, so the duration within this band should be a factor $\ln(1.25/0.65) = 0.65$ of the cooling time.

Figure 15 shows the observed duration of loops versus their density lower bounds. Assuming even modest iron enhancement, $\alpha_{\rm Fe} = 2$, yields a cooling lifetime shorter than most observed durations. With no enhancement at all, $\alpha_{\rm Fe} = 1$, more than a third of the loops last longer than the upper bound on their cooling lifetime. For the value taken as typical of active region loops, $\alpha_{\rm Fe} = 4$ (Aschwanden et al. 2003), every single loop lives longer than its radiative lifetime. All of these comparisons suggests that loops are undergoing some heating throughout their period of 171 Å emission. It is also noteworthy that the density lower bounds all exceed the apex density of a 120 Mm loop in equilibrium, according to Rosner, Tucker, and Vaiana (RTV; Rosner et al. 1978).

Concurrent observations from the *Yohkoh* SXT provide further insight into the energetics of the reconnected loops. Interconnecting structure can be discerned as early as 11:48 on August 10, 2 hr prior to the appearance of loop 1 in the 171 Å data. A generalized brightening over the entire active region complex begins at 5:23 on August 10. Shortly after this there is a very bright knot in the center of the reconnection region (see Fig. 16). By 7:13 this resolves into a single wide looplike structure within the P051–N01 domain, which remains pronounced and bright for $\sim$3 hr.

Partial frame images (PFIs) of the region were made at high time cadence mostly during two intervals. These alternate between filters and therefore may be used to derive temperatures and emission measures. Figure 17 shows the total emission measure and average temperature in each of two distinct regions.

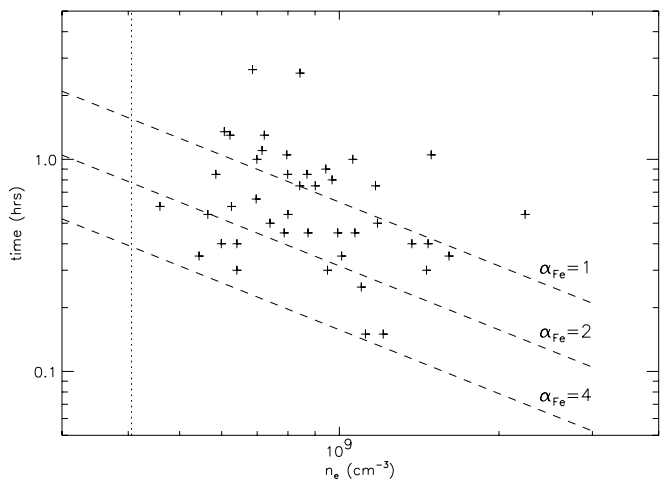

FIG. 15.—Plot of the observed duration of each loop against the lower bound estimate on its average density, n_e. The dashed lines are $0.65\tau_{\rm rad}$ for values of the iron abundance $\alpha_{\rm Fe} = 1$, 2, and 4. The vertical dotted line is the apex density of a coronal loop in RTV equilibrium.

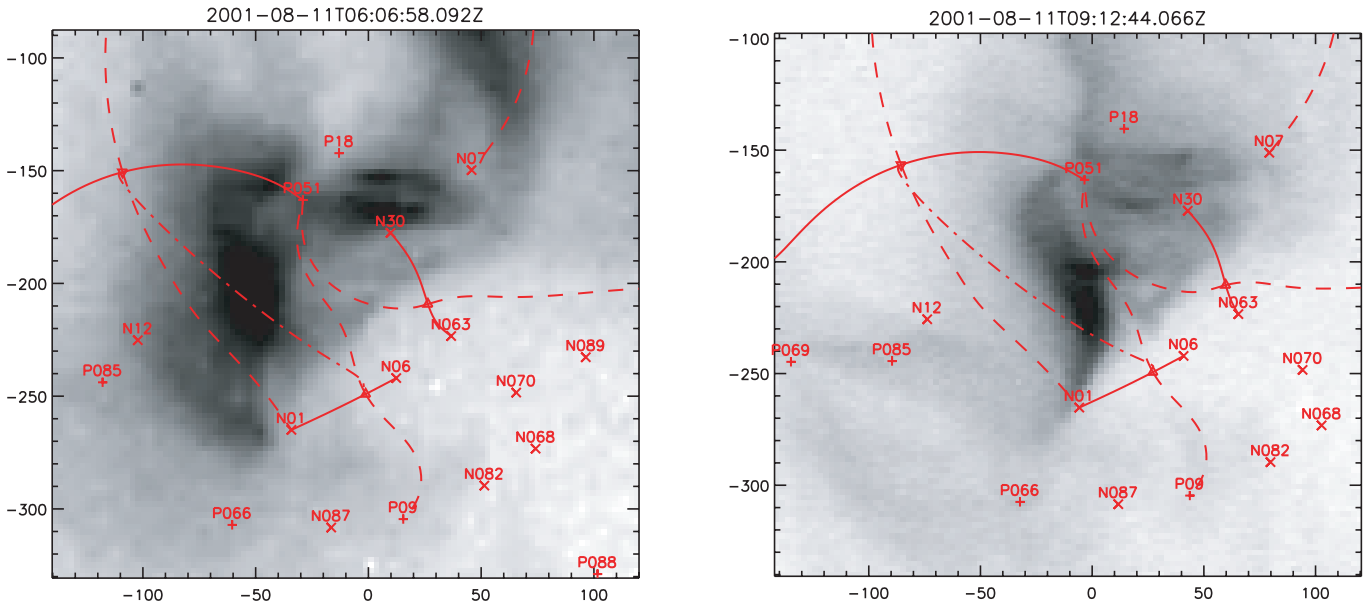

FIG. 16.—Partial frame images from *Yohkoh* SXT at 6:06 (*left*) and 9:12 (*right*) on August 11. The inverse gray scale is square root of intensity (to enhance contrast). Features of the magnetic model are overplotted as in Fig. 12.

Region A includes only the bright east-west loops forming AR 9574; these are the horizontal features centered at $x \simeq 20''$, $y \simeq -170''$ in Figure 16. Region B includes all features in the interconnecting domain. The emission measure and temperature of region A stay roughly constant at EM $\simeq 0.5 \times 10^{48}$ cm^{-3} and $T \simeq 6$ MK. The emission measure of region B is clearly increasing in the first PFI set (beginning at 5:46) and decreasing by the second set (beginning at 9:04). The temperature of region B is above 7.5 MK during its rising phase and has fallen to the same value as region A ($\sim$6 MK) by the second interval. Indeed, the average temperature of region B at 9:15 appears to be steadily falling at a rate $dT/dt \simeq -0.6$ MK hr^{-1} (the fit shown as black dotted line),

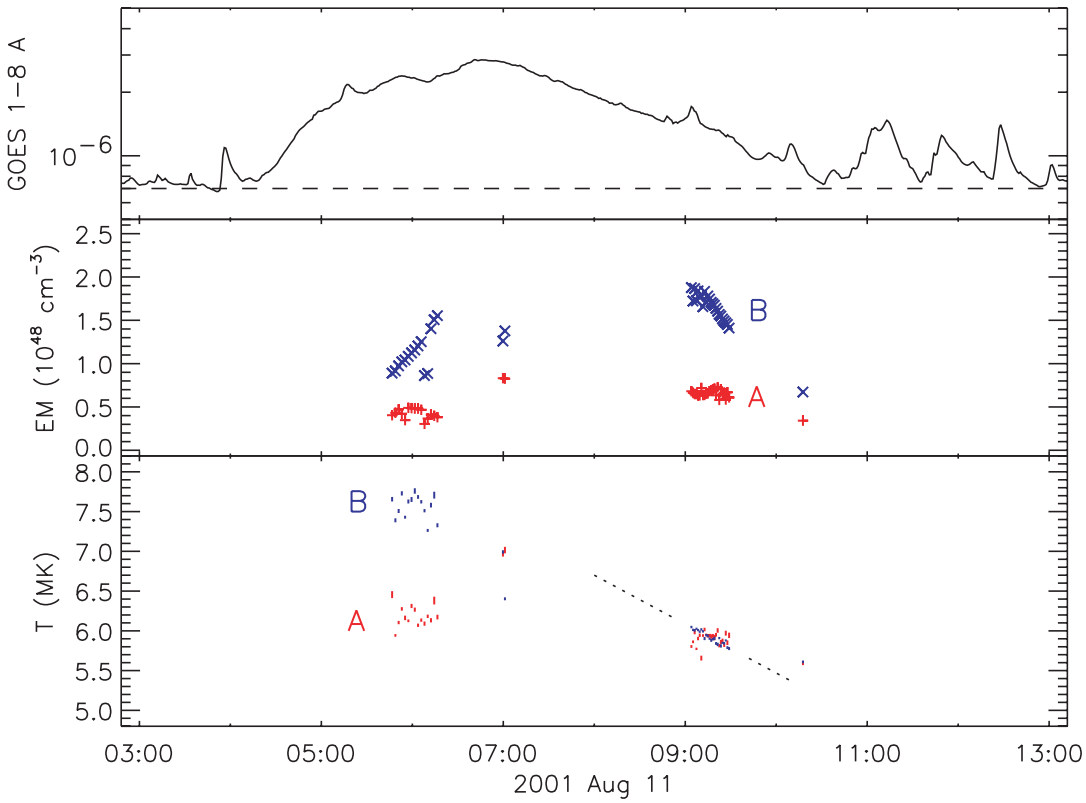

FIG. 17.—Time histories of X-ray–derived quantities at the reconnection episode. The top panel is a section of the same *GOES* curve from Fig. 7. The middle panel shows the total emission measure in region A (*red plus signs*; AR 9574) and region B (*blue crosses*; interconnecting flux) in units of 10^{48} cm^{-3}. The bottom panel shows the average temperatures of the same two regions as vertical error bars denoting the uncertainty. A black dotted line shows a fit to the late cooling trend of region B, $dT/dt = -0.6$ MK hr^{-1}.

in contrast to region A, which appears to be maintaining its 6 MK temperature. All of this is consistent with the scenario that reconnection begins some time after 4:30 and that the reconnected loops (region B) cool gradually over the next 6–8 hr.

We conclude that region B primarily includes emission measure from the reconnected flux. The volume of a reconnected flux tube is the product of its flux $\Delta\psi$ and the integral

$$\mathcal{V} \equiv \int \frac{dl}{|\boldsymbol{B}(l)|} \tag{5}$$

over the axis of the tube. For a field line selected in a manner similar to Figure 13, but at 7:00 on August 11, we find $\mathcal{V} = 1.0$ Mm G^{-1}. If the peak emission measure, EM $= 1.9 \times 10^{48}$ cm^{-3}, corresponds to the entirety of the reconnected flux from Figure 14, $\Delta\psi = 6 \times 10^{20}$ Mx, then it would occupy a volume $V = 6 \times 10^{28}$ cm^3 at an average density of

$$n_e = \sqrt{\frac{\mathrm{EM}}{V}} = \sqrt{\frac{\mathrm{EM}}{\Delta\psi\mathcal{V}}} = 5.6 \times 10^9. \tag{6}$$

Had we used a more conservative estimate of the emitting magnetic flux, $\Delta\psi$, the density estimate would be even higher. Comparison to the 171 Å density estimates indicate that the loops drain to a much lower density by the time they pass through the *TRACE* passband, beginning at 9:00.

At the very high temperatures observed by SXT, the dominant cooling will be by thermal conduction. The conductive cooling time

$$\tau_{\mathrm{cond}} \equiv \frac{3n_e k_{\mathrm{B}}(L/2)^2}{\kappa_0 T^{5/2}} \tag{7}$$

will be 1000 s (0.3 hr) for a $T = 6$ MK plasma at the density just derived. In spite of this, the loops persist for 4–5 hr before fading from SXT and appearing in *TRACE*. Moreover, the observed cooling rate at 9:15 (see Fig. 17) gives an instantaneous cooling time of 10 hr. This slow cooling strongly suggests there is continued heating for considerable time after the reconnection has occurred.

Over this same period the *GOES* 1–8 Å channel, shown along the tops of Figure 7 and 17, rises from its background level $F_{\mathrm{bg}} \sim 7.5 \times 10^{-7}$ W m^{-2}. The rise begins at about 4:30, reaching a peak of $F \simeq 3 \times 10^{-6}$ at 6:45 and then returning to the background level at 10:30. We propose that the 5:00–7:00 period of rising X-ray emission corresponds to the episode of separator reconnection transferring the flux visible at 171 Å 4 hr later, at 9:00. The reconnected flux tubes are filled with very hot plasma which gradually cools, passing first through SXT and then through *TRACE* passbands.

The energy released by reconnection can be estimated from both the EUV and X-ray observations. The total power radiated in all wavelengths is $\mathcal{P}_r$ times the volume V of the loop, where $\mathcal{P}_r$ is taken from expression (4). The total energy needed to keep the loop bright in EUV for τ_{171} is

$$\Delta E = \mathcal{P}_r V(\tau_{171} - \tau_{\mathrm{rad}}), \tag{8}$$

where τ_{rad} is its radiative cooling time, here taken with iron enhancement $\alpha_{\mathrm{Fe}} = 4$, following Aschwanden et al. (2003). The median energy release from the 30 loops brightening between 9:00 and 12:00 is $\Delta E = 6 \times 10^{26}$ ergs; the sum of all 30 energies is $\sum \Delta E = 3.5 \times 10^{28}$ ergs. Since $\mathcal{P}_r$ is found using a lower bound on the electron density n_e, this value is a lower bound on the energy radiated by these interconnecting loops during their appearance in 171 Å.

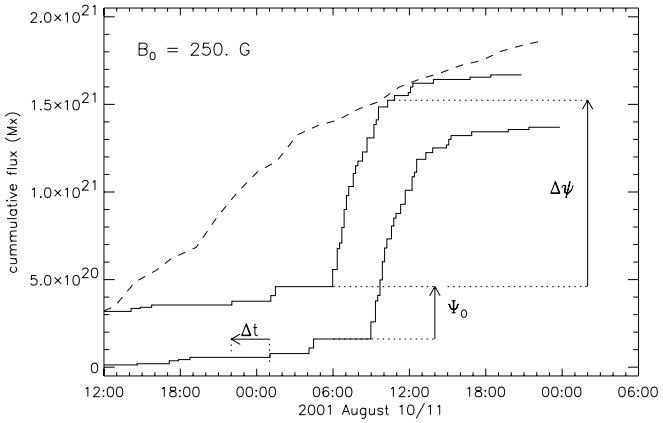

FIG. 18.—Plot of the accumulated loop area multiplied by $B_0/f = 250$ G (*lowest curve*) and the interconnecting flux in a potential field $\psi^{(v)}$ (*dashed curve*). The upper solid curve accounts for a cooling delay and possible unobserved early reconnection by advancing the observations by $\Delta t = 3$ hr and adding $\Psi_0 = \psi^{(v)}(12{:}00)$ to them. The resulting curve reaches $\psi^{(v)}$ following a reconnection episode occurring at 6:00. The extent of the most rapid reconnection is $\Delta\psi = 1.1 \times 10^{21}$ Mx.

An alternative estimate of the radiated energy comes from the *GOES* light curves in both the 1–8 Å (see Fig. 17) and the 0.5–4 Å channels. The pre-event flux (background) of disk-integrated X-rays was approximately 7.5×10^{-7} and 1.2×10^{-8} W m^{-2} in the two channels, respectively. Peak flux occurred near 6:45 UT in both channels: 3.4×10^{-6} and 4.4×10^{-7} W m^{-2}. Using *GOES* analysis software in SolarSoft (Freeland & Handy 1998), a ratio of the channels is compared to the response functions of the *GOES* instrument to estimate the plasma temperature (Thomas et al. 1985; Garcia 1994) at between 5 and 7 MK during the interval of elevated X-ray flux. Based on a synthetic solar spectrum, these temperatures indicate emission measures in the range $(2\text{–}10) \times 10^{48}$ cm^{-3}; this is larger than the SXT value. Integrating over the entire spectrum and over the interval 2:00 –11:00 UT gives a total radiated energy of 2.4×10^{30} ergs.

4.1. *Modeling Energy Storage and Release*

The potential flux $\psi^{(v)}$ is generally taken as an upper bound on the flux that could be reconnected (Longcope 1996). When the observed loop areas are multiplied by the field strength from potential field, $B_0 = 37$ G, they account for much less than this upper bound. This could result from any combination of three basic factors: either the reconnection has transferred less flux than necessary to achieve a potential field, or the flux tube fields are stronger than in the potential extrapolation, or some portion of the reconnected flux is too hot or too faint to be apparent in 171 Å data. The third possibility allows for the largest flux transfer since it is consistent with the flux-transfer upper bound $\psi^{(v)}$. Assuming this in an estimate of reconnection energy release yields the largest possible value, although the estimate itself is a lower bound.

Toward this end we assume that only a fraction f of the flux transferred after 12:00 August 10 is ever visible in 171 Å. To account for the observed cooling delay between SXT and *TRACE* 171 Å, we advance the cumulative area function by $\Delta t = 3$ hr. We find that multiplying the areas by $B_0/f = 250$ G produces a reconnection curve that achieves the potential value $\psi^{(v)}(t)$ following the episode at 6:00 August 11 (see Fig. 18).

The interconnecting flux prior to this episode is smaller than $\psi^{(v)}$ by $\Delta\psi \simeq 1.1 \times 10^{21}$ Mx. We now estimate the energy that could be released by a reconnection episode that transfers this flux in 3 hr. Such a transfer would require a loop voltage $\dot{\psi} = 1.0 \times 10^{17}$ Mx s^{-1}, or 10^9 V.

The potential field is the minimum energy state for a given distribution of photospheric flux. The fact that domain P051–N01 has flux different from $\psi^{(v)}$ means that the field cannot be potential (i.e., it must contain current). The minimum energy state subject to this single observational constraint, the actual flux ψ interconnecting P051–N01, is the *flux constrained equilibrium* (Longcope 2001). This equilibrium is current-free except for a current sheet running along the separator. Large-scale properties of this current sheet, such as width and net current, can be estimated using an expansion about the potential field (Longcope & Silva 1998; Longcope & Magara 2004). (The current density and thickness of the current sheet, on the other hand, would be set by *dynamics* in its vicinity and cannot be predicted using this or any quasi-static model.) In the potential field at 6:00 August 11, the separator B1–A2 is $L = 206.4$ Mm long and has an average shear parameter $I^{\star}/c = 2.4 \times 10^{11}$ G cm (2.4×10^{12} A), found by integrating the perpendicular magnetic shear along the separator of the potential field (see Longcope & Silva 1998; Longcope & Magara 2004 for details). In order to produce a self-flux compensating for $\Delta\psi$, the current sheet must carry a current I satisfying the equation (Longcope & Silva 1998; Longcope & Magara 2004)

$$\Delta\psi = \frac{IL}{c} \ln\left(\frac{eI^{\star}}{|I|}\right), \tag{9}$$

where $e = 2.718$ is the base of the natural logarithm, L is the length of the potential separator, and $I^{\star}$ is its average shear parameter. The solution for the values given above is $I = 0.056\, I^{\star} = 1.34 \times 10^{10} c$ (1.34×10^{11} A).

Due to the flux constraint, this equilibrium has energy greater than the potential field by

$$\Delta W_{\rm FCE} = \frac{1}{2} L \left(\frac{I}{c}\right)^2 \ln\left(\frac{\sqrt{e} I^{\star}}{|I|}\right) = 1.4 \times 10^{31} \text{ ergs}. \tag{10}$$

Since the actual magnetic field is probably subject to constraints in addition to the one on its interconnecting flux, such as line-tying constraints, $\Delta W_{\rm FCE}$ will be a lower bound on the free energy. Each additional constraint will store additional energy, and eliminating the constraint would release this stored energy.

The free-energy estimate in equation (10) follows from the application of a single constraint to the coronal magnetic field. Additional energy $\Delta W_{\rm FCE}$ is required because the total interconnecting flux, ψ, differs from the amount a potential field would have, $\psi^{(v)}$. The state of minimum energy has an infinitely thin current sheet; however, this does not mean, nor do we assume, that the actual magnetic field has a current sheet. The fact that the state of minimum energy contains a current sheet may suggest that the self-consistent dynamics of the coronal field will tend to concentrate current in the vicinity of the separator. Self-consistent, nonlinear dynamics would ultimately determine details of the current distribution such as its thickness (resisitivity, for example, would prevent the formation of a genuine discontinuity). This is, however, a subject far too complex to delve into here. The salient point is that any coronal field with interconnecting flux ψ must contain magnetic energy in excess of the potential field by at least the amount in expression (10), where the current I is set by the flux discrepancy through equation (9).

5. DISCUSSION

The foregoing observation of the emergence of AR 9574 has provided new insight into the process of magnetic reconnection in the corona. These insights follow after the data are interpreted in the context of a magnetic model. The interpretations are not always unambiguous, so some of the results define ranges of possible values.

The simple presence of the interconnecting flux is, by itself, very strong evidence for separator reconnection. Assuming that the interconnecting field has not emerged at the same time as the flux internal to AR 9574, it must be created in the corona by exchanging the footpoints in pairs of field lines: reconnection. This process can only occur through some version of separator reconnection that is the topological analog of X-point reconnection in two dimensions (Longcope & Cowley 1996). The locations of the observed loops, their low densities, their inferred cooling, and the observed energy release all argue against interconnected emergence and therefore in favor of separator reconnection.

The separators in our magnetic model occur because of the distinction we make between the two active regions. Some magnetic models, on the other hand, assume the photospheric magnetic field to be a monolithic, smooth function that cannot be unambiguously divided into regions. This approach eliminates all separators of the type discussed since it prevents categorical distinctions between footpoints. In their place are neighborhoods of distorted field-line mapping known as quasi-separatrix layers (QSLs), which are geometrical rather topological features (Priest & Démoulin 1995). In model problems where the photospheric field is changed from monolithic to discrete, the QSLs in the first case are found to occur at the locations corresponding to the separatrices in the second (Titov et al. 2002). In this sense distinction between active regions might be considered as an approximation used to facilitate the identification of QSLs.

Real active regions do, however, appear to be distinct from one another in many physically meaningful senses. The process of active region emergence, of which AR 9574 is one example, suggests that a distinct entity has risen from an interior layer (Fisher et al. 2000). It is therefore quite natural to adopt a model that distinguishes magnetic footpoints in one active region from those in another. The boundaries between the field lines rooted in these distinct regions become the separatrices, and their intersections are the separators. Once this distinction is made, topological reconnection (separator reconnection) is the only means of changing the amount of flux with a particular topology (Greene 1988; Lau & Finn 1990). Since field lines with an interconnecting topology cannot be produced through emergence, they must result from separator reconnection.

The time history of the 171 Å loops suggests a highly intermittent reconnection process. Most of the reconnection occurs in a 3–6 hr interval whose onset is delayed by approximately 24 hr following the onset of flux emergence. We find nothing in the photospheric flux evolution at that time that could be construed as a trigger for this event. We are left to conclude that the reconnection episode is somehow triggered from the corona after roughly 24 hr of relatively quiet evolution. Some reconnection does occur during the quiet buildup phase, since at least eight different interconnecting loops are visible, the first with incontrovertible connection appearing only 7 hr after the onset of emergence. But the reconnection rate during this period is evidently very low.

All interconnecting loops that we observe are relatively narrow, as is typical of *TRACE* EUV observations. A loop of median

diameter, $d = 3.7$ Mm (still well above the resolution limit), corresponds to a bundle of $\sim 4 \times 10^{18}$ Mx of magnetic flux. One explanation for this structuring is a reconnection process that is also spatially intermittent, or patchy, and reconnects discrete bundles of flux of approximately this size. Prior evidence for patchy reconnection has been found in downflowing plasma voids following eruptive flares (McKenzie 2000) and in flux transfer events in the Earth's magnetosphere (Russell & Elphic 1978). If it is also responsible for setting the size of interconnecting loops, then the present observation provides the first estimate of its scale, at least in nonflaring reconnection.

5.1. *Potential Inaccuracies in the Flux Estimates*

We have used the coronal loops observed at 171 Å to estimate the total flux transferred into the interconnecting domain. There are several uncertainties in this process that prevent us from obtaining a firm value. The most significant uncertainty stems from our inability to measure the magnetic field strength B_0 within the coronal loops. A potential field extrapolated from point sources has a separator with an apex field strength of 30 G. Since interconnecting loops must lie below the separator, and the field is probably not potential, 30 G can be taken as a lower bound on the actual field strength. A field line underneath the separator, whose shape resembles one of the EUV loops (loop 4), has a field strength 37 G at the point it crosses the slit (33 Mm). The field strength increases downward and is $B_0 \simeq 70$ G at a height of 20 Mm. The presence of current in the field could also increase the field strength: in linear force-free fields with $|\alpha| \leq 0.02$ M^{-1}, the field strength at the 33 Mm point is as large as $B_0 \simeq 70$ G. We therefore conclude that the actual field strength within each loop is at least 37 G, but is probably larger by as much as a factor of 2.

The observed coronal loops bear a striking resemblance to the field lines in our potential field extrapolation (see Fig. 12), suggesting that the potential approximation is a reasonable one, at least on the active region scale. In light of this we feel it is unlikely that the true value of B_0 could exceed a value of 37 G by very much. Thus the 43 observed loops appear to account for $(2\text{–}6) \times 10^{20}$ Mx of interconnecting flux. In further discussion we adopt an intermediate value, $\Delta\psi_{171} = 4 \times 10^{20}$ Mx, as the reconnected flux observed in *TRACE* 171 Å.

In order for the magnetic field to remain potential, or even approximately potential, it would need to transfer $\Delta\psi \simeq 1.5 \times 10^{21}$ Mx: 4 times what we observe. It is theoretically possible that the reconnection is incomplete and that the field never fully relaxes. If the interconnecting domain were deprived of 75% of its flux, however, it would be smaller than the potential field, whose separatrices are plotted on the stack plot in Figure 2, by a factor even smaller than one-fourth (that is, one-fourth of the cross section, meaning one-half of the apparent width). During the period of intensive reconnection, however, loops are observed over the entire width spanned by the potential separatrices. This suggests that the interconnecting domain is almost as wide as in the potential field and must therefore contain almost as much magnetic flux.

Where, then, is the rest of the interconnecting flux? There are several ways in which we might have undercounted the flux, even in those loops we did observe. For instance, one continuous streak on the stack plot, which we designate as a single loop, might actually consist of multiple sequential brightenings at closely spaced locations. This possibility, a spiritual relative of the "nanoflare hypothesis," was neglected under assumption 3, that each loop tracks a single bundle of flux. An alternative conjecture, that each loop was actually three or four different loops brightening in rapid succession, would account for the flux discrepancy and also bring the individual durations into agreement with their radiative lifetimes (see Fig. 15). Such a model has been found to fit the observed behavior of active region loops observed in *TRACE* (Warren et al. 2003). In the present observation, however, this hypothesis raises a host of new questions. How do four neighboring flux bundles, all created by reconnection 3–6 hr earlier, suddenly brighten with such well-timed synchronization that they cannot be distinguished from one another?

A more straightforward possibility is that *TRACE* 171 Å observations simply miss much of the flux. One possibility is that 75% of the flux is in loops so narrow ($d < 0.7$ Mm) or containing so little emission measure that they have evaded detection. Unresolved loops within the *TRACE* temperature band would presumably contribute to a diffuse background of emission. We have subtracted from the *TRACE* data the mean background level from the quiet-Sun corona (Cirtain 2005). It is possible that reconnection had such a negligible effect on most of the flux that its intensity remained at or barely above this background level. Figure 7 shows that the majority of emission above the quiet-Sun background level has been attributed to identified loops, especially during the reconnection episode. This seems to leave little room for the remaining 75% of the flux to have been significantly heated from reconnection.

The final possibility is that 75% of the flux in the interconnecting domain never cools to temperatures observable in Fe XI/X emission. This means, in effect, that the 171 Å has a gross filling factor of 25%. This is a reasonable possibility, since many coronal loop equilibrium models suggest that plasma above 2 MK should be relatively common, especially in long loops. It is not clear, however, that we can expect other coronal regions, such as active region fields, to have the same gross filling factor.

5.2. *The Missing Connection*

The absence of a second flux system from the purported reconnection poses a more puzzling instance of missing flux. Due to the nature of magnetic field lines, the act of reconnection should produce two distinct types of field lines. In the present scenario, reconnection will destroy field lines from domains P051–N06 and P057–N01 to create field lines in P051–N01 and P057–N06. This reconnection would be only the final one in a two-stage sequence required to create field lines interconnecting the two regions. Figure 10 shows that the P051–N06 field lines were themselves the product of reconnection along a B1–A3 separator that destroyed P051–N30 flux (in AR 9574) and P057–N06 flux (in AR 9570). Since N06 is so very small, this reconnection must be followed almost immediately by the one we have focused on, which creates P051–N01. We have observed field lines from this domain, but not from the second recipient domain: P057–N06. Where are the field lines of this domain?

The most obvious explanation is that flux in the second domain, P057–N06, is even harder to detect than that of the domain P051–N01, from which we may have missed 75%. Since the first post-reconnection domain lies under the separator, the second will lie above it. A typical field line from the potential model of domain P057–N06 at 6:30 August 11 is 270 Mm: more than twice as long as those typical of P051–N01. In equilibrium these long field lines will be half as dense and thus have one-quarter the emission measure density, n_e^2, of their low-lying counterparts. This typical field line extends to a height of 84 Mm, where its field strength is 10 G, one-quarter the value of the P051–N01 line. The pair of post-reconnection flux tubes will have equal flux, giving the upper one twice the diameter.

Combining their lower density and larger diameter, the field lines from domain P057–N06 will be one-eighth as bright as those of P051–N01. We therefore propose that they would be too faint to be detectable in the present data.

5.3. *Energetics*

Our data are excellent for tallying reconnected flux, but are not ideally suited to quantifying the detailed energetics of the reconnection. We are, however, able to put some constraints on the energy liberation. The interconnecting loops cool gradually after reconnection, suggesting that a significant portion of the energy released is *not* directly converted to heat by the reconnection process. Had the reconnection converted magnetic energy into heat directly, the loops would have cooled freely immediately after entering the interconnecting domain. This is contradicted by the much slower cooling implied by the 3 hr time delay between SXT and *TRACE* 171 Å temperatures and the extended durations of all loops within the 171 Å passband. The slow cooling suggests a continued heating following reconnection, at a gradually diminishing rate.

Following the logic above, the energy liberated by reconnection must have been dissipated (converted to heat) only gradually. All energy that is dissipated must, nevertheless, have been stored as magnetic energy prior to reconnection. The net stored energy must therefore match or exceed the total power dissipated over the extended dissipation period. We used two independent methods to place a lower bound on this integrated power.

The disk-integrated *GOES* X-ray observations can be used to derive the temperature (6–8 MK) and emission measure (2×10^{48} cm^{-2}) during the reconnection episode. The total power radiated by this plasma, over all wavelengths, during its appearance in *GOES* X-rays is estimated to be 2.4×10^{30} ergs. This may include emission from outside the post-reconnection flux or from the P057–N06 domain. Indeed, the SXT images reveal the emerging active region 9574 to have 6 MK plasma amounting to one-half or one-third the emission measure of that seen in domain P051–N01.

An independent estimate comes from the loops observed in 171 Å. The average intensity of each loop was used to provide a lower bound on the electron density, n_e, by assuming that the plasma was at the optimal temperature for Fe XI/X emission. This lower bound was then used in an estimate of the total power density, $\mathcal{P}_r$, radiated over all wavelengths, which is therefore also an underestimate. Integrating the power radiated after 1 cooling time, and summing all loops observed between 9:00 and 12:00, yields 3.5×10^{28} ergs. Unlike the *GOES* X-ray measurement, this value includes only energy dissipated within the post-reconnection domain P051–N01. The value does, however, exclude a majority of the stored energy, even discounting the possibly higher electron densities. The observed loops had radiated most of their energy during the ~3 hr prior to their cooling into the *TRACE* passband, and the loop-based estimate does not include this energy. It appears that a majority of the reconnected flux never cools into the *TRACE* passband, so its radiated energy is omitted altogether.

6. SUMMARY

6.1. *Observations*

The principle coronal observations presented here are high time cadence 171 Å images of the regions between an emerging active region (AR 9574) and an existing region (AR 9570). We identify 43 instances of loops interconnecting these regions in a stack plot. There is at least one loop interconnecting the regions during most of the observation, but most of the loops occur during a 3 hr period. By attributing a single magnetic field strength B_0 to these loops and assuming that each interconnection is evident in 171 Å, we calculated an electromotive force (EMF) from the reconnection between the regions. This curve is small until the 3 hr period of numerous interconnecting loops. Estimates of the plasma density within these loops, along with observations in soft X-rays (*GOES* and *Yohkoh*), indicate that the interconnecting loops are being heated over most of their lives.

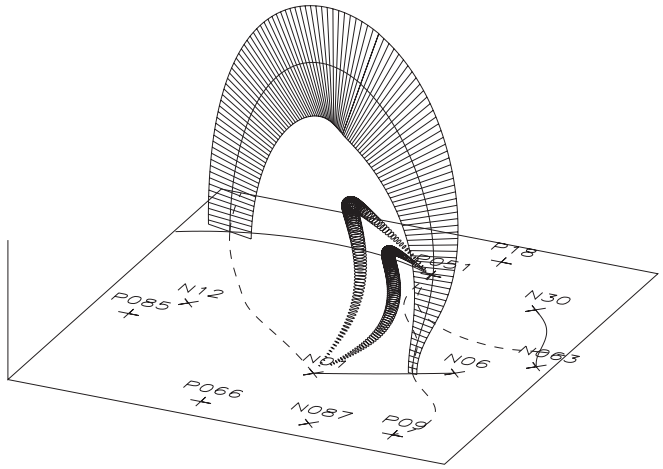

FIG. 19.—Illustration in perspective of the model of the reconnection between AR 9570 and AR 9574. The vertical separator current sheet is shown as a skeleton, and a pair of reconnected flux tubes, 4×10^{18} Mx each, created by patches of reconnection on the separator current sheet lie underneath it.

A magnetic model of the two active regions is constructed from full-disk MDI magnetograms. These were used to model the evolution of 36 distinct regions of concentrated flux. The four concentrations composing the emerging region increased and separated beginning at approximately 7:30 on August 10. The topology of the coronal field was modeled as a potential field anchored in point sources representing each of the concentrations. This model field included a domain of flux interconnecting one concentration (P051) from the emerging region to one (N01) in the preexisting region. The flux in this model domain increases steadily, in contrast to the EMF inferred from the loop observations. The potential field extrapolation provides a value of the interconnecting field strength $B_0 \sim 37$ G, at positions just beneath the magnetic separator. Multiplying the EUV loops by this value results in an interconnecting flux smaller than the model's interconnecting domain by a factor of 4.

6.2. *Interpretation*

To further summarize these observations, we describe the model with which we have succeeded in interpreting the data. This model is offered as a method of organizing the observations and is probably not the only one consistent with the data.

Active region 9574 began emerging at 7:30 August 10 as its 10^{22} Mx flux tube crossed the photosphere, in the neighborhood of existing active region 9570. During the first 24 hr of emergence, reconnection between the active regions proceeded slowly. The lack of reconnection caused magnetic stress to accumulate as current concentrated along the magnetic separator (see Fig. 19). At around 6:00 August 11, when the accumulated current had reached $I \simeq 1.2 \times 10^{11}$ A, a brief reconnection

episode was triggered. The reconnection persisted for 3 hr at an average loop voltage of 10^9 V, leading to the transfer of $\simeq 10^{21}$ Mx across the separator. Localized patches of the separator current underwent reconnection to create flux bundles of $\sim 4 \times 10^{18}$ Mx each. The stressed field had accumulated at least $\Delta W \simeq 1.4 \times 10^{31}$ ergs, which was then released by the reconnection, but very little was dissipated directly at the separator. The released energy was converted instead into small-scale fluctuations such as a turbulence of Alfvén waves or tangled equilibrium field, whose energy was dissipated over the following 6 hr, causing the loops to cool and fade gradually.

This work was supported by NASA grant NAG5-10489. Portions of the work were completed at the Isaac Newton Institute at Cambridge University, where the manuscript benefited from useful comments offered by Klaus Galsgaard, Hugh Hudson, Clare Parnell, and Lidia van Driel-Gesztelyi.

REFERENCES

Antiochos, S. K. 1998, ApJ, 502, L181
Aschwanden, M. J., Nightingale, R. W., & Alexander, D. 2000, ApJ, 541, 1059
Aschwanden, M. J., Schrijver, C. J., Winebarger, A. R., & Warren, H. P. 2003, ApJ, 588, L49
Berger, T. E., de Pontieu, B., Schrijver, C. J., & Title, A. M. 1999, ApJ, 519, L97
Berger, T. E., & Lites, B. W. 2003, Sol. Phys., 213, 213
Bungey, T. N., Titov, V. S., & Priest, E. R. 1996, A&A, 308, 233
Cirtain, J. W. 2005, Ph.D. thesis, Montana State Univ.
Fisher, G. H., Fan, Y., Longcope, D. W., Linton, M. G., & Pevtsov, A. 2000, Sol. Phys., 192, 119
Fletcher, L., & Hudson, H. 2001, Sol. Phys., 204, 69
Freeland, S. L., & Handy, B. N. 1998, Sol. Phys., 182, 497
Garcia, H. A. 1994, Sol. Phys., 154, 275
Golub, L., Krieger, A. S., Harvey, J. W., & Vaiana, G. S. 1977, Sol. Phys., 53, 111
Greene, J. M. 1988, J. Geophys. Res., 93, 8583
Handy, B. N., et al. 1999, Sol. Phys., 187, 229
Lau, Y.-T., & Finn, J. M. 1990, ApJ, 350, 672
Longcope, D. W. 1996, Sol. Phys., 169, 91
———. 2001, Phys. Plasmas, 8, 5277
Longcope, D. W., & Cowley, S. C. 1996, Phys. Plasmas, 3, 2885
Longcope, D. W., & Klapper, I. 2002, ApJ, 579, 468
Longcope, D. W., & Magara, T. 2004, ApJ, 608, 1106
Longcope, D. W., & Silva, A. V. R. 1998, Sol. Phys., 179, 349
McKenzie, D. E. 2000, Sol. Phys., 195, 381
———. 2002, in Multi-Wavelength Observations of Coronal Structure and Dynamics, ed. P. C. H. Martens & D. Cauffman (Amsterdam: Pergamon), 155
Parker, E. N. 1972, ApJ, 174, 499
Pevtsov, A. A. 2000, ApJ, 531, 553
Priest, E. R., & Démoulin, P. 1995, J. Geophys. Res., 100, 23443
Rosner, R., Tucker, W. H., & Vaiana, G. S. 1978, ApJ, 220, 643
Russell, C. T., & Elphic, R. C. 1978, Space Sci. Rev., 22, 681
Scherrer, P. H., et al. 1995, Sol. Phys., 162, 129
Sheeley, N. R., Bohlin, J. D., Brueckner, G. E., Purcell, J. D., Scherrer, V., & Tousey, R. 1975, Sol. Phys., 40, 103
Sweet, P. A. 1958, Nuovo Cimento, 8, 188
Thomas, R. J., Crannell, C. J., & Starr, R. 1985, Sol. Phys., 95, 323
Titov, V. S., Hornig, G., & Démoulin, P. 2002, J. Geophys. Res., 107(A8), SSH 3-1
Tsuneta, S. 1996, ApJ, 456, L63
Tsuneta, S., et al. 1991, Sol. Phys., 136, 37
Warren, H. P., Winebarger, A. R., & Mariska, J. T. 2003, ApJ, 593, 1174